

TransGUNet: Transformer Meets Graph-based Skip Connection for Medical Image Segmentation

Ju-Hyeon Nam Nur Suriza Syazwany Sang-Chul Lee*
 Department of Electrical and Computer Engineering, Inha University
 100, Inha-ro, Michuhol-gu, Incheon, Republic of Korea
 {jhnam0514, surizasyazwany, sclee}@inha.edu

Abstract

Skip connection engineering is primarily employed to address the semantic gap between the encoder and decoder, while also integrating global dependencies to understand the relationships among complex anatomical structures in medical image segmentation. Although several models have proposed transformer-based approaches to incorporate global dependencies within skip connections, they often face limitations in capturing detailed local features with high computational complexity. In contrast, graph neural networks (GNNs) exploit graph structures to effectively capture local and global features. Leveraging these properties, we introduce an attentional cross-scale graph neural network (ACS-GNN), which enhances the skip connection framework by converting cross-scale feature maps into a graph structure and capturing complex anatomical structures through node attention. Additionally, we observed that deep learning models often produce uninformative feature maps, which degrades the quality of spatial attention maps. To address this problem, we integrated entropy-driven feature selection (EFS) with spatial attention, calculating an entropy score for each channel and filtering out high-entropy feature maps. Our innovative framework, **TransGUNet**, comprises ACS-GNN and EFS-based spatial attention to effectively enhance domain generalizability across various modalities by leveraging GNNs alongside a reliable spatial attention map, ensuring more robust features within the skip connection. Through comprehensive experiments and analysis, TransGUNet achieved superior segmentation performance on six seen and eight unseen datasets, demonstrating significantly higher efficiency compared to previous methods.

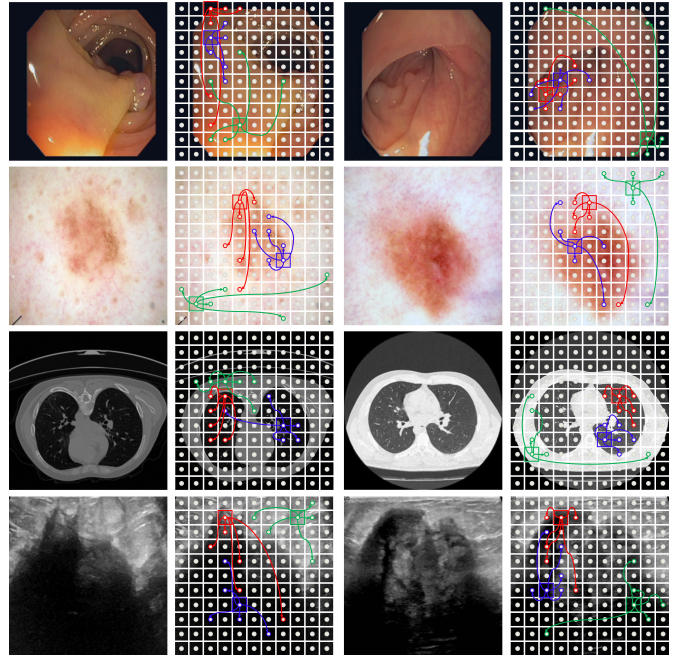


Figure 1. Graph Visualization of TransGUNet. We selected three patches (Red, Blue, Green) and found the five nearest patches for each, based on the adjacency matrix of ACS-GNN, connecting them with lines to visualize the relationships using each color. This figure reveals that lesion patches exhibit high similarity with other lesion patches, while non-lesion patches similarly cluster together. This result demonstrates the model’s effectiveness in distinguishing lesion from non-lesion regions and maintaining strong intra-class correlations.

1. Introduction

Medical image segmentation is crucial for the early detection of abnormal tissues and the development of treatment plans [9]. Traditional segmentation algorithms have received considerable attention from medical experts [23,

* denotes the corresponding author.

32, 47, 57]. However, these methods still lack generalizability owing to the severe noise, inhomogeneous intensity distribution, and various clinical settings in medical images [51]. Consequently, this issue has raised concerns about the reliability of computer-based diagnostic procedures [18].

Recently, convolutional neural networks (CNNs) have been widely employed for medical image segmentation owing to their robustness in capturing local and spatial hierarchical features [44, 52, 77]. However, CNN-based models struggle to capture the global dependencies necessary to understand the complex anatomical structures in medical images [24]. This limitation has expanded the use of transformers to extract global dependencies for medical image segmentation [5, 7]. However, despite their strengths, transformer-based models often fail to bridge the semantic gap between the encoder and decoder, hindering their ability to fully leverage global dependencies and resulting in sub-optimal segmentation performance [64].

Several models have been actively employed to improve skip connections to reduce this semantic gap for medical image segmentation. The most representative of these attempts is UNet++ [79], which uses cross-scale feature fusion through dense connectivity in skip connection. Similarly, UCTransNet [64] and CFATransUNet [63] adopted a transformer-based approach to capture local cross-channel interactions of feature maps from a channel-wise perspective. However, these models suffer from increased computational complexity and ambiguous attention owing to their dense connectivity, extensive use of transformer blocks, and complex background in medical images with severe noise. Consequently, addressing the question, “*How can we efficiently leverage global dependency without ambiguity while reducing the semantic gap between the encoder and decoder?*” is critical to overcoming these challenges and improving performance for medical image segmentation.

To answer this question, we focused on graph neural networks (GNNs), which are particularly suitable for flexibly and effectively capturing local and global dependencies, making them ideal for complex visual perception tasks [21]. By leveraging this capability, we propose an *attentional cross-scale GNN (ACS-GNN)* that can efficiently reduce the semantic gap between the encoder and decoder. It transforms cross-scale feature maps into graphs and applies attention to each node to facilitate robust feature integration. Additionally, we observed that deep learning models often produce uninformative feature maps that degrade the quality of spatial attention maps [8, 53]. To address this issue, we introduce an *entropy-driven feature selection (EFS)*, which calculates entropy per channel and filters out high-entropy channels. By integrating *ACS-GNN* and *EFS-based spatial attention*, we designed a new medical image segmentation model called **TransGUNet** which effectively captures the relationships between patches, regardless

of the lesion size and distance between patches (Fig. 1). Extensive experimental results demonstrate that our graph-based approach consistently outperforms transformer- and convolution-based methods. Thus, TransGUNet represents a significant advancement in skip connection frameworks for medical image segmentation and offers a robust and efficient solution to the existing challenges. The main contributions of this study can be summarized as follows:

- We propose **TransGUNet**, a novel medical image segmentation model that leverages the cross-scale GNN-based skip connection framework without ambiguous spatial attention and is applicable to various modalities and clinical settings. To the best of our knowledge, our novel skip connection framework is the first study to successfully and effectively exploit attentional cross-scale GNN with non-ambiguous spatial attention for medical image segmentation.
- The proposed *attentional cross-scale graph neural network (ACS-GNN)* allows the model to comprehend the complex anatomical structures within medical images. Additionally, we incorporated *entropy-driven feature selection (EFS)* with spatial attention to produce more reliable spatial attention maps.
- Our experimental results demonstrate that TransGUNet significantly outperforms transformer- and convolution-based approaches employed for medical image segmentation with various clinical settings.

2. Related Works

Skip Connection Engineering for Medical Image Segmentation. The introduction of skip connections in UNet marked a significant milestone and made it the most widely used baseline model in medical image segmentation. However, there is still a semantic gap between the encoder and decoder, which results in suboptimal performance [38]. This problem has driven recent efforts to refine skip connections to minimize this semantic gap. UNet++ is a representative model incorporating dense connectivity and neighbor scale features in skip connections. Additionally, MSNet [77] and M2SNet [78] reduce redundant features using subtraction modules to design more efficient models. Recently, transformers have been employed as skip connection modules to capture the global dependencies in medical images [17, 26]. Notably, UCTransNet [64], FCT [58], and CFATransUNet [63] maintain global dependency by leveraging transformer-based skip connection frameworks. However, these models have complex architectures with more than **60M parameters**, which can be computationally expensive and inefficient. Our innovative TransGUNet addresses these challenges by utilizing cross-scale GNN with node attention and reducing the semantic gap with a significantly more efficient architecture comprising **25M parameters**. We compare the schemes and properties of various skip connection

Skip Connection Properties		UNet (MICCAI2016)	UNet++ (DLMIA2018)	M2SNet (arxiv2023)	ViGUNet (ISBI2023)	CFATUNet (CBM2024)	PVT-GCAS (WACV2024)	GSENet (BSPC2025)	TransGUNet (Ours)
Full Global Dependency		-	-	-	✓	✓	-	✓	✓
Cross-Scale Fusion		-	✓	✓	✓	✓	-	✓	✓
Non-Ambiguous Spatial Attention		-	-	-	-	-	-	-	✓
Efficiency	Params (M)	8.2	34.9	25.3	2.3	64.6	25.4	26.9	25.0
	FLOPs (G)	23.7	197.8	12.8	5.0	32.9	7.9	17.4	10.0
	Inference Speed (ms)	18.6	26.5	34.9	25.1	36.0	17.4	37.5	19.4
	Required GPU Memory (G)	0.4	1.2	0.6	3.1	1.0	0.4	0.5	0.4

Table 1. Comparison of skip connection frameworks characteristics among UNet, UNet++, M2SNet, ViGUNet, CFATransUNet (CFATUNet), PVT-GCASCAD (PVT-GCAS), GSENet, and **TransGUNet (Ours)**.

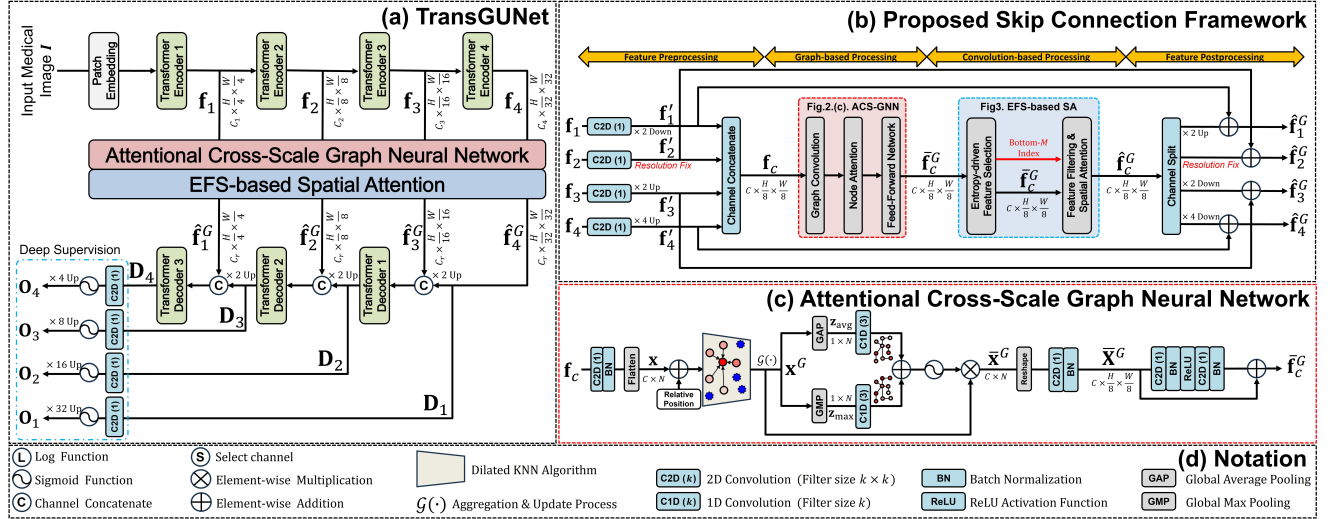


Figure 2. (a) The overall architecture of the proposed TransGUNet mainly comprises ACS-GNN and EFS-based spatial attention (See Fig. 3). (b) The proposed novel skip connection framework. In this figure, we set the target resolution as $(H_t, W_t) = (\frac{H}{8}, \frac{W}{8})$. And, for convenience, we assume that $C = 4C_r$. (c) Overall block diagram of the proposed ACS-GNN. (d) Notation description used in this paper. This notation is also used in Fig. 3.

frameworks in Tab. 1 and Appendix (Fig. 8).

GNNs for Computer Vision. GNNs have been traditionally employed for natural language processing [33] and recommendation systems [73] owing to their ability to comprehend intricate relationships within datasets. Recently, in computer vision, GNNs [21, 22] have been actively explored to flexibly extract global dependencies and local features based on graphs, which are generalized data structures encompassing grids (CNN) and sequences (Transformer). For example, SFDGNet [68] extracts content-specific manipulated frequency features using GNN and comprehends complex spatial and frequency relationships. Additionally, GazeGNN [62] integrates raw eye-gaze data and images into a unified representation graph for real-time disease classification. In particular, ViGUNet [29] and PVT-GCASCAD [50] utilize GNNs to handle complex anatomical structures in medical image segmentation. Additionally, GTBA-Net [72], TSGCNet [12], MSAGANet [69], TGNet [75], and GSENet [36] tried to combine transformer and GNN for medical image segmentation. However, these

models do not consider cross-scale features and lack a reliable spatial attention map. Noting these limitations, we carefully designed TransGUNet, which incorporates cross-scale features through ACS-GNN with EFS-based reliable spatial attention and fully utilizes global dependency.

3. Method

3.1. Encoder and Decoder in TransGUNet

We used a Pyramid Pooling Transformer (P2T) [70] comprising multiple pooling-based multi-head self-attention. P2T incurs a significantly lower computational cost and higher representation power than Vision Transformer (ViT) and Pyramid Vision Transformer (PVT), which are adopted in various medical image segmentation models [10, 37, 76]. Inspired by previous studies, we utilized the same encoder architecture as the decoder to fully leverage global dependency. Although we primarily present the experimental results using P2T, we also provide various CNN and transformer backbones to demonstrate the versatility and robust-

ness of the proposed approach across different backbone architectures in the Appendix (Tab. 9).

3.2. ACS-GNN with EFS-based spatial attention for Skip Connection

Motivation: The human visual system (HVS) recognizes objects by dividing them into large parts and understanding them based on the connectivity strengths of each part [39]. This process helps interpret complex scenes by identifying relationships between different parts of an image, leading to a holistic understanding of objects and their interactions [41, 48]. Inspired by these principles, our approach employs a similar strategy of the HVS by transforming the cross-scale feature map into graphs to understand the complex anatomical structures in a high-dimensional feature space. However, significant noise and complex backgrounds create highly ambiguous visual signals that disturb the neural systems. The HVS mitigates this issue through signal filtering and attention processing [49, 59]. Therefore, we propose an entropy-based feature selection strategy that mimics these feature filtering and attention processes, called EFS-based spatial attention. The integration of these components enhances the preservation of global dependencies and the local details without ambiguity in attention mechanism. The overall architecture of the TransGUNet is illustrated in Fig. 2. The ACS-GNN with EFS-based spatial attention can be divided into four steps: 1) *Feature Preprocessing*, 2) *ACS-GNN* (Fig. 2 (c)), 3) *EFS-based spatial attention* (Fig. 3), and 4) *Feature Postprocessing*.

Feature Preprocessing. Let $\mathbf{f}_i \in \mathbb{R}^{C_i \times \frac{H}{2^{i+1}} \times \frac{W}{2^{i+1}}}$ be the feature maps from the i -th encoder stage for $i = 1, 2, 3, 4$ where (H, W) is the resolution of the input image. Because the number of channels in each stage primarily affects the complexity of the decoder, we employed a 2D convolution with a kernel size of 1×1 to reduce the number of channels to C_r . To obtain the cross-scale feature map \mathbf{f}_c , we resized them to the same resolution for $i = 1, 2, 3, 4$ as follows:

$$\mathbf{f}'_i = \mathbf{Resize}_{(H_t, W_t)}(\mathbf{C2D}_{1 \times 1}(\mathbf{f}_i)) \in \mathbb{R}^{C_r \times H_t \times W_t} \quad (1)$$

where $\mathbf{C2D}_{k \times k}(\cdot)$, and $\mathbf{Resize}_{(H_t, W_t)}(\cdot)$ denote the 2D convolution with a kernel size of $k \times k$, and an operation to resize into the target spatial resolution (H_t, W_t) , respectively. If the target and original resolutions of the input feature map differ, bilinear interpolation is used to upsample or downsample feature map to match the target resolution. Alternatively, if they have the same resolution, we do not apply resize, denoted as “*Resolution Fix*” in Fig. 2 (b). And then, we concatenate each resized feature map $\mathbf{f}_c = [\mathbf{f}'_1, \mathbf{f}'_2, \mathbf{f}'_3, \mathbf{f}'_4] \in \mathbb{R}^{4C_r \times H_t \times W_t}$ where $[\dots]$ denotes concatenation between feature maps along the channel dimension. For convenience, we assume that $C = 4C_r$.

Attentional Cross-Scale Graph Neural Network. After obtaining the cross-scale feature map $\mathbf{f}_c \in \mathbb{R}^{C \times H_t \times W_t}$, we apply

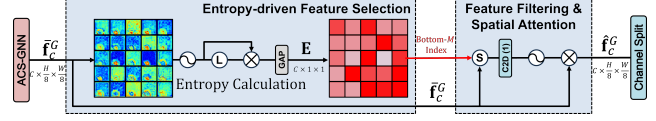


Figure 3. The overall block diagram of the Entropy-driven Feature Selection with spatial attention. Low and high transparency red indicates a high and low entropy score, respectively. We produce the spatial attention map using the indices corresponding to the M channels with the lowest entropy scores, called Bottom- M index.

2D convolution with a kernel size of 1×1 and batch normalization (BN). Subsequently, the feature map is converted into a flattened vector $\mathbf{x} \in \mathbb{R}^{C \times N}$, where $N = H_t W_t$. Each pixel in \mathbf{x} acts as a node in the graph. Additionally, a relative positional vector is added to each flattened vector element to preserve the position information. Next, we constructed the feature graph using the dilated K -nearest neighbors (KNN) algorithm. To implement the exchange of information between nodes, we adopted the Max-Relative graph convolution (MRConv) [34] owing to its simplicity and efficiency as it does not require learnable parameters for node aggregation. The MRConv and Update processes are implemented for graph convolution as $\mathbf{x}^G = \mathcal{G}(\mathbf{x})$.

To improve feature aggregation by adaptively weighting the node importance, we applied node attention to prioritize critical features while learning their relevance. Based on ECANet [65], we designed a node attention mechanism using a single 1D convolution operation with kernel size of k and sigmoid function. Firstly, \mathbf{x}^G is compressed into \mathbf{z}_{avg} and \mathbf{z}_{max} using Global Average Pooling and Global Max Pooling, respectively, and then each statistic is aggregated to produce a node attention map. Finally, such an attention mechanism is readily implemented as follows:

$$\bar{\mathbf{x}}^G = \mathbf{x}^G \times \sigma \left(\sum_{d \in \{\text{avg}, \text{max}\}} \mathbf{C1D}_k(\mathbf{z}_d) \right) \quad (2)$$

where $\mathbf{C1D}_k(\cdot)$ and $\sigma(\cdot)$ denote 1D convolution with a kernel size of k and the sigmoid function, respectively. And, we reshape flattened vector $\bar{\mathbf{x}}^G$ into original feature map shape and apply 2D convolution with a kernel size of 1×1 and BN for more nonlinearity to obtain the refined feature map $\bar{\mathbf{X}}^G \in \mathbb{R}^{C \times H_t \times W_t}$. To address the oversmoothing problem [35, 46] in GNN, we also utilize Feed-Forward Networks with two consecutive convolutional layers and residual connections as follows:

$$\bar{\mathbf{f}}_c^G = \mathbf{BN}(\mathbf{C2D}_{1 \times 1}(\delta(\mathbf{BN}(\mathbf{C2D}_{1 \times 1}(\bar{\mathbf{X}}^G)))))) + \bar{\mathbf{X}}^G \quad (3)$$

where $\delta(\cdot)$ and $\mathbf{BN}(\cdot)$ denote the ReLU activation function for non-linearity and batch normalization, respectively.

Spatial Attention with Entropy-driven Feature Selection. Although a GNN can maintain global dependencies,

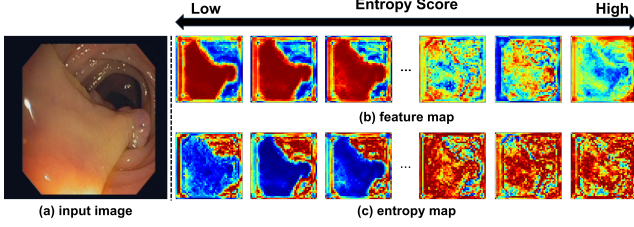


Figure 4. (a) Input image, (b) Feature map from ACS-GNN, (c) Entropy map according to each feature map. We calculated entropy map using Shannon Entropy at pixel level.

various noise and complex backgrounds in medical images still result in an uninformative feature map containing a high-entropy score, leading to a poor spatial attention map [8, 53]. To address this issue, we propose *entropy-driven feature selection (EFS)-based spatial attention*, which illustrated in Fig. 3, that filters uninformative feature maps and generates a more reliable spatial attention map. We observed that the channel with a high entropy is uniformly or noisily activated as shown in Fig. 4. Therefore, inspired by previous studies [61, 66], we calculated the entropy score $\mathbf{E} \in \mathbb{R}^C$ at the pixel level for each channel of the input feature map using Shannon Entropy as follows:

$$\mathbf{E} = \frac{1}{HW} \sum_{h=1}^H \sum_{w=1}^W (-\sigma(\bar{\mathbf{f}}_c^G)_{:,h,w} \log(\sigma(\bar{\mathbf{f}}_c^G)_{:,h,w})) \quad (4)$$

Subsequently, we only retained the feature map channels with the M lowest entropy scores and used them for spatial attention as follows:

$$\hat{\mathbf{f}}_c^G = \bar{\mathbf{f}}_c^G \times \sigma(\mathbf{C2D}_{1 \times 1}((\bar{\mathbf{f}}_c^G)_{\text{sorting}(\mathbf{E})[:M]})) \quad (5)$$

where $\text{sorting}(\cdot)$ denotes the sorting algorithm into ascending. Hence, $\text{sorting}(\mathbf{E})[:M]$ means the Bottom- M index of feature map $\bar{\mathbf{f}}_c^G$ with low entropy score. We used the Introselect algorithm, the default sorting algorithm in PyTorch. This dual process of ACS-GNN and EFS-based spatial attention allows our model to comprehend the intricate anatomical structures in medical images and generate more reliable spatial attention maps.

Feature Postprocessing. We first divided $\hat{\mathbf{f}}_c^G$ along the channel dimension with an equal number of channels C_r . Subsequently, each feature map was resized and applied residual connection between the original feature map to enhance the training stability for $i = 1, 2, 3, 4$ as follows:

$$\hat{\mathbf{f}}_i^G = \mathbf{f}'_i + \text{Resize}_{\left(\frac{H}{2^{i+1}}, \frac{W}{2^{i+1}}\right)} \left((\hat{\mathbf{f}}_c^G)_{C_r \cdot (i-1) : C_r \cdot i} \right) \quad (6)$$

For convenience, let $\mathbf{D}_1 = \hat{\mathbf{f}}_4^G$. Then, we produce the decoder block output \mathbf{D}_{i+1} for $i = 1, 2, 3$ as $\mathbf{D}_{i+1} = \text{Decoder}_i \left(\left[\hat{\mathbf{f}}_{4-i}^G, \text{Up}_2(\mathbf{D}_i) \right] \right)$ where $\text{Up}_n(\cdot)$ and

$\text{Decoder}_i(\cdot)$ denote a bilinear upsampling with scale factor 2^{n-1} and i -th transformer decoder block, respectively. We summarized the technical novelty and impact of TransGUNet in the Appendix.

3.3. Training Procedure

We employed a multi-task learning with deep supervision to enhance the representation power of the model and mitigate the gradient vanishing problem. To implement this, we obtained four predictions \mathbf{O}_i from \mathbf{D}_i for $i = 1, 2, 3, 4$ by applying 2D convolution with kernel size of 1×1 following sigmoid function and upsampling at each stage. We denote $\mathbf{O}_i = \{\mathbf{R}_i, \mathbf{B}_i\}$ as the multiple outputs representing region \mathbf{R}_i and boundary \mathbf{B}_i predictions, respectively. The total loss function is defined as:

$$\mathcal{L}_{total} = \sum_{i=1}^4 (\mathcal{L}_R(\mathbf{R}_t, \mathbf{R}_i) + \mathcal{L}_B(\mathbf{B}_t, \mathbf{B}_i)) \quad (7)$$

where \mathbf{R}_t and \mathbf{B}_t denote the ground truths of region and the boundary, respectively. We obtained \mathbf{B}_t by applying an anisotropic Sobel edge detection filter [31] to \mathbf{R}_t . The loss function for region prediction was defined as $\mathcal{L}_R = \mathcal{L}_{IoU}^w + \mathcal{L}_{bce}^w$, where \mathcal{L}_{IoU}^w and \mathcal{L}_{bce}^w are the weighted IoU and binary cross entropy (BCE) loss functions, respectively. This loss function is identically defined in previous studies [15, 45, 78]. Additionally, we defined boundary loss function \mathcal{L}_B as the BCE loss function.

4. Experiment Results

4.1. Experiment Settings

Each model was trained and evaluated on five medical segmentation tasks, including multi-organ, skin cancer, COVID-19 infection, breast tumors, and polyp. For convenience, we denote the *seen* clinical settings (Tab. 2) as the test dataset, which has the same distribution with the training dataset. Moreover, we additionally evaluate the domain generalizability of each model on eight external segmentation datasets using different distributions for the training and test datasets, which are referred to as *unseen* clinical settings (Tab. 3). Due to the page limit, we present the detailed dataset description and split information in the Appendix (Tab. 6 and 7). To evaluate the performance of each model, we selected two metrics, the Dice Score Coefficient (DSC) and mean Intersection over Union (mIoU), which are widely used in medical image segmentation. Additionally, the quantitative results with more various metrics are also available in the Appendix.

We compared the proposed **TransGUNet (Ours)** with twelve representative medical image segmentation models, including UNet [52], UNet++ [79], CENet [19], TransUNet [7], MSRFNet [55], DCSAUNet [71], M2SNet [78], ViGUNet [29], PVT-GCAS [50], CFATUNet [63], MADGNet

Method	Synapse [3]		ISIC2018 [20]		COVID19-1 [30]		BUSI [2]		CVC-ClinicDB [4]		Kvasir-SEG [27]		P-value
	DSC	mIoU	DSC	mIoU	DSC	mIoU	DSC	mIoU	DSC	mIoU	DSC	mIoU	
UNet [52]	69.8 (0.6)	58.9 (0.4)	86.9 (0.8)	80.2 (0.7)	47.7 (0.6)	38.6 (0.6)	69.5 (0.3)	60.2 (0.2)	76.5 (0.8)	69.1 (0.9)	80.5 (0.3)	72.6 (0.4)	9.3E-06
UNet++ [79]	79.3 (0.2)	69.8 (0.1)	87.3 (0.2)	80.2 (0.1)	65.6 (0.7)	57.1 (0.8)	72.4 (0.1)	62.5 (0.2)	79.7 (0.2)	73.6 (0.4)	84.3 (0.3)	77.4 (0.2)	4.0E-05
CENet [19]	75.2 (0.3)	64.6 (0.4)	89.1 (0.2)	82.1 (0.1)	76.3 (0.4)	69.2 (0.5)	79.7 (0.6)	65.0 (0.5)	89.3 (0.3)	83.4 (0.2)	89.5 (0.7)	83.9 (0.7)	7.1E-07
TransUNet [7]	77.5 (0.2)	67.1 (0.6)	87.3 (0.2)	81.2 (0.8)	75.6 (0.4)	68.8 (0.2)	75.5 (0.5)	68.4 (0.1)	87.4 (0.2)	82.4 (0.1)	86.4 (0.4)	80.1 (0.4)	4.5E-09
MSRFNet [55]	77.2 (0.5)	67.6 (0.3)	88.2 (0.2)	81.3 (0.2)	75.2 (0.4)	68.0 (0.4)	76.6 (0.7)	68.1 (0.7)	83.2 (0.9)	76.5 (1.1)	86.1 (0.5)	79.3 (0.4)	1.0E-07
DCSAUNet [71]	71.0 (0.3)	55.8 (0.1)	89.0 (0.3)	82.0 (0.3)	75.3 (0.4)	68.2 (0.4)	73.7 (0.5)	65.0 (0.5)	80.6 (1.2)	73.7 (1.1)	82.6 (0.5)	75.2 (0.5)	5.4E-08
M2SNet [78]	77.1 (0.1)	67.5 (0.4)	89.2 (0.2)	83.4 (0.2)	81.7 (0.4)	74.7 (0.5)	80.4 (0.8)	72.5 (0.7)	92.2 (0.8)	88.0 (0.8)	91.2 (0.5)	86.1 (0.6)	2.2E-05
ViGUNet [29]	72.3 (1.5)	67.7 (1.2)	88.3 (1.2)	81.3 (0.1)	70.2 (0.3)	62.1 (0.3)	70.9 (0.2)	61.3 (0.1)	77.5 (0.4)	69.7 (0.7)	79.6 (0.6)	71.3 (0.6)	3.8E-08
PVT-GCAS [50]	78.4 (0.3)	68.9 (0.2)	90.6 (0.3)	84.2 (0.5)	82.3 (0.4)	74.8 (0.5)	82.0 (0.5)	73.6 (0.5)	92.2 (0.6)	87.6 (0.6)	91.6 (0.2)	86.8 (0.4)	1.8E-04
CFATUNet [63]	80.5 (1.4)	70.4 (1.8)	90.3 (0.4)	83.6 (0.7)	80.4 (0.5)	73.6 (0.2)	80.6 (0.3)	72.8 (0.4)	91.0 (0.2)	86.2 (0.1)	92.1 (0.5)	87.2 (0.5)	3.2E-05
MADGNet [45]	79.3 (1.2)	69.8 (1.3)	90.2 (0.1)	83.7 (0.2)	83.7 (0.2)	76.8 (0.2)	81.3 (0.4)	73.4 (0.5)	93.9 (0.6)	89.5 (0.5)	90.7 (0.8)	85.3 (0.8)	6.5E-02
GSENet [36]	79.1 (1.6)	69.2 (1.7)	90.7 (0.2)	84.2 (0.2)	80.7 (0.3)	73.7 (0.4)	80.6 (0.4)	72.8 (0.5)	91.5 (0.2)	86.4 (0.1)	92.1 (0.3)	87.2 (0.4)	3.2E-02
TransGUNet	80.9 (0.4)	71.4 (0.2)	91.1 (0.3)	84.8 (0.4)	84.0 (0.2)	77.0 (0.5)	82.7 (0.3)	74.7 (0.4)	92.3 (0.2)	87.7 (0.4)	93.1 (0.1)	88.4 (0.2)	-
	+0.4	+1.0	+0.5	+0.6	+0.3	+0.2	+0.7	+1.1	-1.6	-1.8	+1.0	+1.2	

Table 2. Segmentation results on six different datasets with *seen* clinical settings. (·) denotes the standard deviations of multiple experiment results. We also provide the Wilcoxon signed rank test results (P -value) compared to our method and other methods.

Method	AMOS-CT [28]		AMOS-MRI [28]		PH2 [42]		COVID19-2 [1]		STU [80]		CVC-300 [60]		CVC-Colon [56]		ETIS [54]		P-value
	DSC	mIoU	DSC	mIoU	DSC	mIoU	DSC	mIoU	DSC	mIoU	DSC	mIoU	DSC	mIoU	DSC	mIoU	
UNet [52]	56.3 (2.1)	44.8 (1.4)	8.3 (2.5)	5.3 (1.9)	90.3 (0.1)	83.5 (0.1)	47.1 (0.7)	37.7 (0.6)	71.6 (1.0)	61.6 (0.7)	66.1 (2.3)	58.5 (2.1)	56.8 (1.3)	49.0 (1.2)	41.6 (1.1)	35.4 (1.0)	1.7E-08
UNet++ [79]	67.5 (2.3)	56.6 (2.8)	6.0 (1.2)	3.8 (1.5)	88.0 (0.3)	80.1 (0.3)	50.5 (3.3)	40.9 (3.7)	77.3 (0.4)	67.8 (0.3)	64.4 (2.2)	58.4 (2.0)	57.5 (0.4)	50.2 (0.4)	39.1 (2.4)	34.0 (2.1)	3.1E-07
CENet [19]	67.9 (2.3)	56.5 (2.4)	14.5 (1.4)	9.0 (1.6)	90.5 (0.1)	83.3 (0.1)	60.1 (0.3)	49.9 (0.3)	86.0 (0.7)	77.2 (0.9)	85.4 (1.6)	78.2 (1.4)	65.9 (1.6)	59.2 (0.1)	57.0 (3.4)	51.4 (0.5)	1.8E-05
TransUNet [7]	68.3 (1.1)	57.7 (1.2)	9.1 (2.3)	5.8 (2.5)	89.5 (0.3)	82.1 (0.4)	56.9 (1.0)	48.0 (0.7)	41.4 (4.5)	32.1 (4.2)	85.0 (0.6)	77.3 (0.3)	63.7 (0.1)	58.4 (0.3)	50.1 (0.5)	44.0 (2.3)	7.3E-06
MSRFNet [55]	61.8 (1.3)	51.3 (1.7)	6.5 (2.3)	4.2 (1.9)	90.5 (0.3)	83.5 (0.3)	58.3 (0.8)	48.4 (0.6)	84.0 (5.5)	75.2 (5.2)	72.3 (2.2)	65.4 (2.2)	61.5 (1.0)	54.8 (0.8)	38.3 (0.6)	33.7 (0.7)	5.6E-06
DCSAUNet [71]	45.7 (1.2)	36.3 (1.5)	1.7 (0.5)	1.1 (0.2)	89.0 (0.4)	81.5 (0.3)	52.4 (1.2)	44.0 (0.7)	86.1 (0.5)	76.5 (0.8)	68.9 (4.0)	59.8 (3.9)	57.8 (0.4)	49.3 (0.4)	43.0 (3.0)	36.1 (2.9)	6.9E-07
M2SNet [78]	69.6 (1.3)	58.5 (0.5)	22.0 (0.6)	14.7 (0.8)	90.7 (0.3)	83.5 (0.5)	68.6 (0.1)	58.9 (0.2)	79.4 (0.7)	69.3 (0.6)	90.0 (0.2)	83.2 (0.3)	75.8 (0.7)	68.5 (0.5)	74.9 (1.3)	67.8 (1.4)	1.3E-04
ViGUNet [29]	50.8 (2.7)	42.8 (2.3)	6.5 (0.2)	4.5 (0.3)	90.1 (0.7)	82.8 (0.5)	49.7 (0.3)	41.9 (0.4)	75.5 (1.2)	65.0 (1.1)	72.9 (0.4)	62.8 (0.2)	53.7 (0.6)	53.7 (0.7)	38.6 (3.1)	31.6 (2.2)	3.9E-09
PVT-GCAS [50]	69.3 (1.4)	58.5 (1.6)	32.8 (2.4)	24.3 (2.2)	91.5 (1.3)	84.9 (1.5)	71.0 (0.4)	60.4 (0.4)	86.4 (0.6)	76.6 (0.2)	88.2 (0.4)	81.0 (0.5)	79.5 (0.9)	71.6 (0.9)	79.5 (0.7)	71.6 (1.0)	3.9E-04
CFATUNet [63]	68.0 (2.6)	56.7 (2.1)	35.9 (3.2)	25.9 (3.6)	91.5 (0.6)	85.0 (0.7)	65.7 (1.2)	56.2 (1.1)	87.9 (0.1)	79.2 (0.2)	89.1 (0.6)	82.4 (0.6)	78.0 (0.9)	70.3 (0.8)	77.0 (0.6)	69.5 (0.7)	8.8E-05
MADGNet [45]	74.9 (1.2)	64.4 (1.3)	14.8 (2.5)	9.8 (2.7)	91.3 (0.1)	84.6 (0.1)	72.2 (0.1)	62.6 (0.3)	88.4 (1.0)	79.9 (1.5)	87.4 (0.4)	79.9 (0.4)	77.5 (1.1)	69.7 (1.2)	77.0 (0.3)	69.7 (0.5)	1.3E-02
GSENet [36]	74.2 (0.2)	63.4 (0.4)	36.3 (4.0)	27.2 (3.5)	91.5 (0.3)	85.0 (0.4)	66.3 (0.3)	56.5 (0.4)	86.3 (0.4)	76.7 (0.5)	89.0 (0.1)	82.1 (0.1)	80.1 (1.4)	71.9 (1.2)	79.3 (0.4)	71.2 (0.3)	1.2E-02
TransGUNet	76.5 (0.5)	66.2 (0.4)	47.2 (1.1)	35.6 (1.2)	91.7 (0.3)	85.2 (0.2)	73.0 (0.2)	62.4 (0.2)	87.4 (0.1)	78.2 (0.4)	90.0 (0.3)	83.1 (0.1)	82.0 (0.2)	74.1 (0.3)	81.3 (0.3)	73.1 (0.2)	-
	+1.6	+1.8	+10.9	+8.4	+0.2	+0.2	+0.8	-0.2	-1.0	-1.7	+0.0	-0.1	+1.9	+2.2	+1.8	+1.5	

Table 3. Segmentation results on eight different datasets with *unseen* clinical settings. (·) denotes the standard deviations of multiple experiment results. We also provide the Wilcoxon signed rank test results (P -value) compared to our method and other methods.

[45], and GSENet [36]. In all results, we report the mean performance of three trials for reliability. In all tables, **Bold** and *italic* are the first and second best performance results, respectively. And, the last row in Tab. 2 and 3 indicates the performance gap between **TransGUNet** and other second best method.

4.2. Implementation Details

We implemented TransGUNet on a single NVIDIA RTX 3090 Ti in Pytorch 1.8.

Multi-Organ Segmentation. Following the previous literature [63], we employ an Adam optimizer with a learning rate of 0.001 for multi-organ segmentation. We optimize each model using a batch size of 24 and train them for 150 epochs. During training, we used flipping with a probability of 50% and rotation between -20° and 20° . Because volumes in *seen* and *unseen* clinical settings have different resolutions, all images were resized to 224×224 . We would like to clarify that we used identical settings in CFATUNet, which is the most recent multi-organ segmentation model. Note that we utilize the same settings on the multi-organ segmentation task to train all models for fair comparison.

Binary Segmentation. We started with an initial learning rate of 10^{-4} using the Adam optimizer and reduced the

parameters of each model to 10^{-6} using a cosine annealing learning rate scheduler. We optimized each model using a batch size of 16 and trained them for 50, 100, 100, and 200 epochs on polyp, skin cancer, breast tumors, and COVID-19 infection segmentation tasks. In the training process, horizontal and vertical flips were applied with a 50% probability, along with rotations ranging from -5° to 5° , as part of a multi-scale training strategy. This approach is commonly utilized in medical image segmentation models [15, 45, 77, 78]. Because images in each dataset have different resolutions, all images were resized to 352×352 . Additionally, we would like to clarify that we used identical settings in M2SNet and MADGNet, which are the most representative medical image segmentation methods.

Hyperparameters of TransGUNet. Key hyperparameters for TransGUNet on all datasets were set to $C_r = 64$ for efficiency and $(H_t, W_t) = (\frac{H}{8}, \frac{W}{8})$, $K = 11$, $k = 3$ in ACS-GNN and $M = 64$ in EFS-based spatial attention. In the Appendix, we provide the experiment results on various hyperparameter settings (Tab. 9, 5, 10, 11).

4.3. Comparison with State-of-the-art models

We used the same model as that in Tab. 2 to evaluate the domain generalizability for unseen clinical settings Tab.

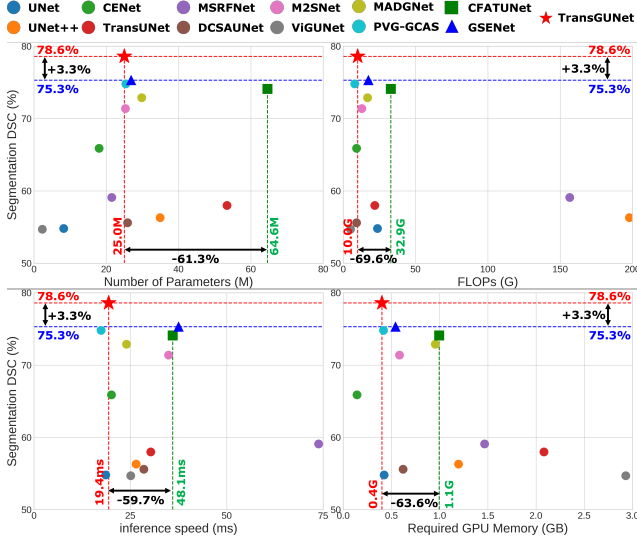


Figure 5. Comparison of parameters (M), FLOPs (G), inference speed (ms), and required GPU memory (G) vs segmentation performance (DSC) on average for all *unseen* datasets.

3. For convenience, we denote (\cdot, \cdot) as the performance improvement gap between TransGUNet and other models for seen and unseen clinical settings. As listed in Tab. 2 and 3, TransGUNet achieved the highest segmentation performance across all various datasets on average. Compared to UNet++, M2SNet, and CFATransUNet, which focus on enhancing the skip connection framework, TransGUNet exhibited DSC improvements of (9.3%, 22.3%), (2.1%, 7.2%), and (1.6%, 4.5%), respectively. Additionally, compared to PVT-GCASCADe, which uses a single-scale GNN with spatial attention, TransGUNet demonstrated DSC improvement of (1.2%, 3.8%). Although MADGNet achieved the state-of-the-art performance in seen clinical settings, TransGUNet exhibited significant DSC improvement of 5.6% for unseen clinical settings on average. Surprisingly, only TransGUNet achieved a DSC over 45% on AMOS-MRI (MRI modality) when trained on Synapse (CT modality). These results indicate that employing an attentional cross-scale GNN-based skip connection with non-ambiguous spatial attention is crucial for understanding complex anatomical structures in medical images. Fig. 5 indicates that TransGUNet contains almost 25.0M parameters with 10.0G FLOPs, which has apparent advantages regarding computational efficiency. We provide detailed number of parameters, FLOPs, and Inference Time (ms) for each model in Appendix (Tab. 8).

Fig. 6 illustrates the qualitative results of the various models. UNet, CENet, MSRFNet, and DCSAUNet, which do not incorporate global dependencies or reduce the semantic gap between the encoder and decoder, produce noisy and unreliable predictions. Despite the advantage of UNet++ and M2SNet for reducing the semantic gap through

Setting Name	GNN			<i>Seen</i>		<i>Unseen</i>		Param (M)	FLOPs (G)
	Single	Cross	NA	DSC	mIoU	DSC	mIoU		
S0				90.6	84.5	82.8	75.4	24.3M	8.9G
S1	✓			92.1	87.3	82.4	74.5	24.4M	9.3G
S2	✓		✓	92.3	87.6	82.7	75.4	24.4M	9.3G
S3		✓		92.2	87.6	83.5	75.8	25.0M	10.0G
S4 (Ours)		✓	✓	92.7	88.1	84.4	76.8	25.0M	10.0G

Table 4. Ablation study of ACS-GNN in skip connection on *Seen* and *Unseen* polyp segmentation datasets. ‘Single’, ‘Cross’, and ‘NA’ denote Single-Scale GNN, Cross-Scale GNN, and Node Attention, respectively.

nested convolution and subtraction units, respectively, their predictions remain for unreliable in colonoscopy images comprising complex polyp structures or ultrasounds containing severe noise. Although TransUNet uses global dependency, it is not employed in the decoder, resulting in inaccurate predictions. CFATransUNet improves upon the previous methods by reducing the semantic gap and incorporating transformer blocks at the decoding stage. However, it overlooks crucial spatial relationships and misses the essential fine and local details needed to interpret medical images effectively. Although PVT-GCASCADe mitigates these deficiencies to a certain extent, it fails to consider cross-scale interactions, reliable spatial attention and the importance of each node in the graph. Furthermore, as illustrated in Fig. 1, TransGUNet can understand the relationships between semantically similar patches regardless of their distance. Consequently, despite the severe noise, lesions of various sizes, and complex anatomical structures in various modalities, TransGUNet produces reliable predictions due to the dual utilization of ACS-GNN and EFS-based spatial attention. More various qualitative results are available in the Appendix (Fig. 9, 10, 11, 12).

4.4. Ablation Study on TransGUNet

We conducted ablation studies on polyp segmentation task to demonstrate the effectiveness of ACS-GNN and EFS-based spatial attention. We want to clarify that the experiment settings for the ablation study are identical to the main experiments for fair comparison.

Ablation Study on ACS-GNN. As listed in Tab. 4, our approach (S4) exhibited the best performance across all settings. S0 represents TransGUNet without an ACS-GNN. The most notable result is that the application of skip connections in GNN, whether single-scale (S1) or cross-scale (S3), improves the performance on the seen dataset. However, on the unseen dataset, the single-scale GNN exhibits a 0.4% performance decrease whereas the cross-scale GNN exhibits a 0.7% performance improvement. These experimental results explain the reason behind TransGUNet outperforming PVT-GCASCADe. Additionally, NA improved the performance of both single-scale (S2) and cross-scale (S4) GNNs, with a negligible increase in the number

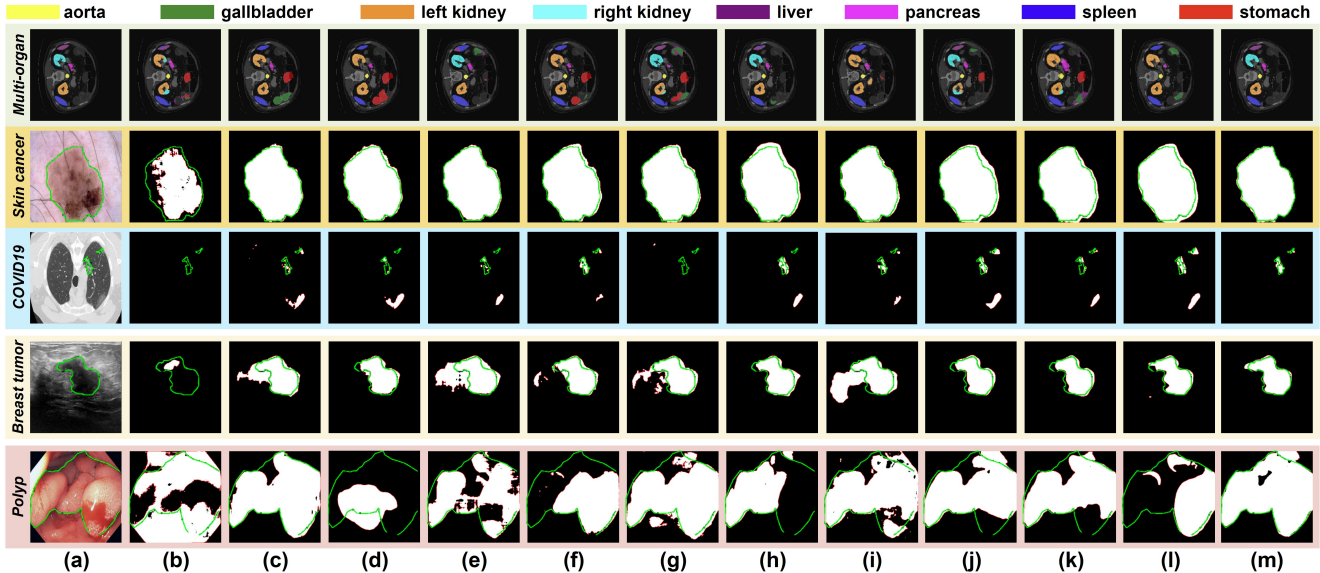


Figure 6. Qualitative comparison of other methods and TransGUNet. (a) Input images with ground truth. (b) UNet [52]. (c) UNet++ [79]. (d) CENet [19]. (e) TransUNet [7]. (f) MSRFNet [55]. (g) DCSAUNet [71]. (h) ViGUNet [29]. (i) M2SNet [78]. (j) PVT-GCASCADE [50]. (k) CFATransUNet [63]. (l) MADGNet [45]. (m) GSENet [36]. (n) **TransGUNet (Ours)**. **Green** and **Red** lines denote the boundaries of the ground truth and prediction, respectively.

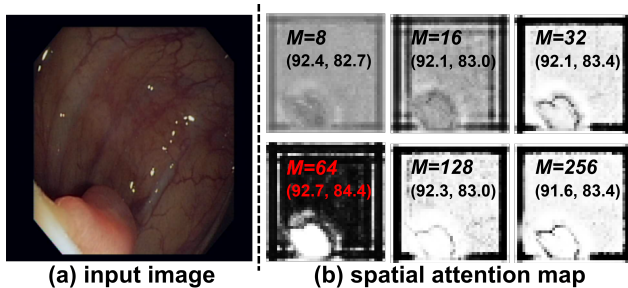


Figure 7. Comparison of spatial attention map quality according to various $M = \{8, 16, 32, 64, 128, 256\}$. (a) Input image, (b) Spatial attention map according to various M .

of parameters and FLOPs owing to the ECA-style attention mechanism. Consequently, TransGUNet, which employs ACS-GNN, performs significantly better across various modalities and clinical settings.

Ablation Study on EFS-based Spatial Attention. As mentioned in the implementation details section, because we set $C_r = 64$, the total number of channels in the skip connection equals $4C_r = 256$. Therefore, when $4C_r = M$, where M is the number of selected channels, all the feature maps are used to produce a spatial attention map. In Fig. 7, (\cdot, \cdot) denotes DSC on seen and unseen clinical setting of polyp segmentation. Fig. 7 shows that $M = 256$ results in worse performance than the cases utilizing the EFS-based spatial attention ($M = \{8, 16, 32, 64, 128\}$). These results demonstrate that our feature selection approach improves

Target Resolution (H_t, W_t)	Seen		Unseen		Param (M)	FLOPs (G)
	DSC	mIoU	DSC	mIoU		
$(H/4, W/4)$	87.1	80.5	78.5	69.7	25.0M	13.6G
$(H/8, W/8)$ (Ours)	87.3	80.6	78.6	69.7	25.0M	10.0G
$(H/16, W/16)$	86.3	79.6	77.2	68.2	25.0M	9.2G
$(H/32, W/32)$	86.2	79.4	76.6	67.7	25.0M	9.0G

Table 5. Quantitative results for each *Seen* and *Unseen* datasets according to various target resolution (H_t, W_t) .

the quality of spatial attention, an aspect not previously addressed. If we select fewer channels ($M = \{8, 16, 32\}$), uncertainty in the spatial attention map increases due to a lack of information.

Ablation Study on Target Resolution in ACS-GNN. In this section, we conduct an ablation study to compare the performance and efficiency according to various target resolution $(H_t, W_t) = \{(H/4, W/4), (H/8, W/8), (H/16, W/16), (H/32, W/32)\}$. Each resolution correspond to the resolutions of the feature maps $\mathbf{f}_i \in \mathbb{R}^{C_i \times \frac{H}{2^{i+1}} \times \frac{W}{2^{i+1}}}$ extracted from the Transformer encoder for $i = 1, 2, 3, 4$. We used $(H/8, W/8)$ as a target resolution (H_t, W_t) . As listed in Tab. 5, the experimental results indicate that the resolution $(H/8, W/8)$ achieved the best performance. Although $(H/4, W/4)$ also demonstrated high performance, the efficiency significantly decreased due to the increased FLOPs associated with the higher resolution of the input feature maps and the inherent characteristics of GNNs. This indicates that while higher resolutions can capture more detailed information, they come at the cost of increased computational resources.

5. Conclusion

In this study, we proposed TransGUNet, an innovative medical image segmentation model that integrates ACS-GNN and EFS-based spatial attention. The proposed model effectively addresses the limitations of the existing models by reducing the semantic gap between the encoder and decoder, preserving crucial information without ambiguous spatial attention, and leveraging global dependencies. Through extensive experiments on six seen and eight unseen datasets, TransGUNet demonstrated superior performance and higher efficiency than the state-of-the-art models. The results of ablation study demonstrate that incorporating GNNs into skip connection engineering significantly enhances the model's ability to capture and utilize complex anatomical features. Additionally, EFS ensures that only the most informative features are considered, thereby improving the quality of spatial attention maps. Consequently, TransGUNet represents a significant advancement in medical image segmentation, offering a robust, efficient, and accurate model that can be employed in various medical applications. In future work, we will focus on optimizing the memory efficiency and explore its deployment in real-world healthcare settings.

References

- [1] Covid19 dataset. <https://www.kaggle.com/datasets/piyushsamant11/pidata-new-names>. 6
- [2] Walid Al-Dhabyani, Mohammed Gomaa, Hussien Khaled, and Aly Fahmy. Dataset of breast ultrasound images. *Data in brief*, 28:104863, 2020. 6, 1, 7, 9
- [3] Landman Bennett, Xu Zhoubing, Igelsias Juan, Styner Martin, Langerak Thomas, and Klein Arno. Segmentation outside the cranial vault challenge. In *Medical Image Computing and Computer-Assisted Intervention—MICCAI 2015: 18th International Conference, Munich, Germany, October 5-9, 2015, Proceedings, Part III 18*. Springer, 2015. 6, 1, 11, 12
- [4] Jorge Bernal, F Javier Sánchez, Gloria Fernández-Esparrach, Debora Gil, Cristina Rodríguez, and Fernando Vilariño. Wm-dova maps for accurate polyp highlighting in colonoscopy: Validation vs. saliency maps from physicians. *Computerized medical imaging and graphics*, 43:99–111, 2015. 6, 1, 8, 10
- [5] Hu Cao, Yueyue Wang, Joy Chen, Dongsheng Jiang, Xiaopeng Zhang, Qi Tian, and Manning Wang. Swin-unet: Unet-like pure transformer for medical image segmentation. In *European conference on computer vision*, pages 205–218. Springer, 2022. 2
- [6] Adrian Celaya, Beatrice Riviere, and David Fuentes. A generalized surface loss for reducing the hausdorff distance in medical imaging segmentation. *arXiv preprint arXiv:2302.03868*, 2023. 4
- [7] Jieneng Chen, Yongyi Lu, Qihang Yu, Xiangde Luo, Ehsan Adeli, Yan Wang, Le Lu, Alan L Yuille, and Yuyin Zhou. Transunet: Transformers make strong encoders for medical image segmentation. *arXiv preprint arXiv:2102.04306*, 2021. 2, 5, 6, 8
- [8] Kecheng Chen, Kun Long, Yazhou Ren, Jiayu Sun, and Xiaorong Pu. Lesion-inspired denoising network: Connecting medical image denoising and lesion detection. In *Proceedings of the 29th ACM International Conference on Multimedia*, pages 3283–3292, 2021. 2, 5
- [9] Alan S Coates, Eric P Winer, Aron Goldhirsch, Richard D Gelber, Michael Gnant, M Piccart-Gebhart, Beat Thürlimann, H-J Senn, Panel Members, Fabrice André, et al. Tailoring therapies—improving the management of early breast cancer: St gallen international expert consensus on the primary therapy of early breast cancer 2015. *Annals of oncology*, 26(8):1533–1546, 2015. 1
- [10] Bo Dong, Wenhai Wang, Deng-Ping Fan, Jinpeng Li, Huazhu Fu, and Ling Shao. Polyp-pvt: Polyp segmentation with pyramid vision transformers. *arXiv preprint arXiv:2108.06932*. 3
- [11] Alexey Dosovitskiy, Lucas Beyer, Alexander Kolesnikov, Dirk Weissenborn, Xiaohua Zhai, Thomas Unterthiner, Mostafa Dehghani, Matthias Minderer, Georg Heigold, Sylvain Gelly, Jakob Uszkoreit, and Neil Houlsby. An image is worth 16x16 words: Transformers for image recognition at scale. In *International Conference on Learning Representations*, 2021. 3
- [12] Fan Duan and Li Chen. 3d dental mesh segmentation using semantics-based feature learning with graph-transformer. In *International Conference on Medical Image Computing and Computer-Assisted Intervention*, pages 456–465. Springer, 2023. 3
- [13] Deng-Ping Fan, Ming-Ming Cheng, Yun Liu, Tao Li, and Ali Borji. Structure-measure: A new way to evaluate foreground maps. In *Proceedings of the IEEE international conference on computer vision*, pages 4548–4557, 2017. 4
- [14] Deng-Ping Fan, Cheng Gong, Yang Cao, Bo Ren, Ming-Ming Cheng, and Ali Borji. Enhanced-alignment measure for binary foreground map evaluation. *arXiv preprint arXiv:1805.10421*, 2018. 4
- [15] Deng-Ping Fan, Ge-Peng Ji, Tao Zhou, Geng Chen, Huazhu Fu, Jianbing Shen, and Ling Shao. Pranut: Parallel reverse attention network for polyp segmentation. In *International conference on medical image computing and computer-assisted intervention*, pages 263–273. Springer, 2020. 5, 6
- [16] Shang-Hua Gao, Ming-Ming Cheng, Kai Zhao, Xin-Yu Zhang, Ming-Hsuan Yang, and Philip Torr. Res2net: A new multi-scale backbone architecture. *IEEE transactions on pattern analysis and machine intelligence*, 43(2):652–662, 2019. 3
- [17] Yunhe Gao, Mu Zhou, and Dimitris N Metaxas. Utnet: a hybrid transformer architecture for medical image segmentation. In *Medical Image Computing and Computer Assisted Intervention—MICCAI 2021: 24th International Conference, Strasbourg, France, September 27–October 1, 2021, Proceedings, Part III 24*, pages 61–71. Springer, 2021. 2
- [18] Susanne Gaube, Harini Suresh, Martina Raue, Alexander Merritt, Seth J Berkowitz, Eva Lerner, Joseph F Coughlin,

- John V Guttag, Errol Colak, and Marzyeh Ghassemi. Do as ai say: susceptibility in deployment of clinical decision-aids. *NPJ digital medicine*, 4(1):31, 2021. 2
- [19] Zaiwang Gu, Jun Cheng, Huazhu Fu, Kang Zhou, Huaying Hao, Yitian Zhao, Tianyang Zhang, Shenghua Gao, and Jiang Liu. Ce-net: Context encoder network for 2d medical image segmentation. *IEEE transactions on medical imaging*, 38(10):2281–2292, 2019. 5, 6, 8
- [20] David Gutman, Noel CF Codella, Emre Celebi, Brian Helba, Michael Marchetti, Nabin Mishra, and Allan Halpern. Skin lesion analysis toward melanoma detection: A challenge at the international symposium on biomedical imaging (isbi) 2016, hosted by the international skin imaging collaboration (isic). *arXiv preprint arXiv:1605.01397*, 2016. 6, 1, 5, 9
- [21] Kai Han, Yunhe Wang, Jianyuan Guo, Yehui Tang, and Enhua Wu. Vision gnn: An image is worth graph of nodes. *Advances in neural information processing systems*, 35:8291–8303, 2022. 2, 3
- [22] Yan Han, Peihao Wang, Souvik Kundu, Ying Ding, and Zhangyang Wang. Vision hgnn: An image is more than a graph of nodes. In *Proceedings of the IEEE/CVF International Conference on Computer Vision*, pages 19878–19888, 2023. 3
- [23] Robert M Haralick, Stanley R Sternberg, and Xinhua Zhuang. Image analysis using mathematical morphology. *IEEE transactions on pattern analysis and machine intelligence*, (4):532–550, 1987. 1
- [24] Ali Hatamizadeh, Yucheng Tang, Vishwesh Nath, Dong Yang, Andriy Myronenko, Bennett Landman, Holger R Roth, and Daguang Xu. Unetr: Transformers for 3d medical image segmentation. In *Proceedings of the IEEE/CVF winter conference on applications of computer vision*, pages 574–584, 2022. 2
- [25] Kaiming He, Xiangyu Zhang, Shaoqing Ren, and Jian Sun. Deep residual learning for image recognition. In *Proceedings of the IEEE conference on computer vision and pattern recognition*, pages 770–778, 2016. 3
- [26] Moein Heidari, Amirhossein Kazerooni, Milad Soltany, Reza Azad, Ehsan Khodapanah Aghdam, Julien Cohen-Adad, and Dorit Merhof. Hiformer: Hierarchical multi-scale representations using transformers for medical image segmentation. In *Proceedings of the IEEE/CVF Winter Conference on Applications of Computer Vision*, pages 6202–6212, 2023. 2
- [27] Debesh Jha, Pia H Smedsrud, Michael A Riegler, Pål Halvorsen, Thomas de Lange, Dag Johansen, and Håvard D Johansen. Kvasir-seg: A segmented polyp dataset. In *MultiMedia Modeling: 26th International Conference, MMM 2020, Daejeon, South Korea, January 5–8, 2020, Proceedings, Part II 26*, pages 451–462. Springer, 2020. 6, 1, 8, 10
- [28] Yuanfeng Ji, Haotian Bai, Chongjian Ge, Jie Yang, Ye Zhu, Ruimao Zhang, Zhen Li, Lingyan Zhanng, Wanling Ma, Xiang Wan, et al. Amos: A large-scale abdominal multi-organ benchmark for versatile medical image segmentation. *Advances in neural information processing systems*, 35:36722–36732, 2022. 6, 1, 11, 12
- [29] Juntao Jiang, Xiyu Chen, Guanzhong Tian, and Yong Liu. Vig-unet: vision graph neural networks for medical image segmentation. In *2023 IEEE 20th International Symposium on Biomedical Imaging (ISBI)*, pages 1–5. IEEE, 2023. 3, 5, 6, 8
- [30] Ma Jun, Ge Cheng, Wang Yixin, An Xingle, Gao Jiantao, Yu Ziqi, Zhang Minqing, Liu Xin, Deng Xueyuan, Cao Shucheng, Wei Hao, Mei Sen, Yang Xiaoyu, Nie Ziwei, Li Chen, Tian Lu, Zhu Yuntao, Zhu Qiongjie, Dong Guoqiang, and He Jian. COVID-19 CT Lung and Infection Segmentation Dataset. 2020. 6, 1, 9
- [31] Nick Kanopoulos, Nagesh Vasanthavada, and Robert L Baker. Design of an image edge detection filter using the sobel operator. *IEEE Journal of solid-state circuits*, 23(2): 358–367, 1988. 5
- [32] Michael Kass, Andrew Witkin, and Demetri Terzopoulos. Snakes: Active contour models. *International journal of computer vision*, 1(4):321–331, 1988. 2
- [33] Thomas N Kipf and Max Welling. Semi-supervised classification with graph convolutional networks. *arXiv preprint arXiv:1609.02907*, 2016. 3
- [34] Guohao Li, Matthias Muller, Ali Thabet, and Bernard Ghanem. Deepgcns: Can gcns go as deep as cnns? In *Proceedings of the IEEE/CVF international conference on computer vision*, pages 9267–9276, 2019. 4
- [35] Qimai Li, Zhichao Han, and Xiao-Ming Wu. Deeper insights into graph convolutional networks for semi-supervised learning. In *Proceedings of the AAAI conference on artificial intelligence*, 2018. 4
- [36] Xiang Li, Chong Fu, Qun Wang, Wenchao Zhang, Chen Ye, and Tao Ma. Gse-nets: Global structure enhancement decoder for thyroid nodule segmentation. *Biomedical Signal Processing and Control*, 102:107340, 2025. 3, 6, 8
- [37] Guoqi Liu, Sheng Yao, Dong Liu, Baofang Chang, Zongyu Chen, Jiajia Wang, and Jiangqi Wei. Cafe-net: Cross-attention and feature exploration network for polyp segmentation. *Expert Systems with Applications*, 238:121754, 2024. 3
- [38] Tanvir Mahmud, Md Awsafur Rahman, Shaikh Anowarul Fattah, and Sun-Yuan Kung. Covsegnet: A multi encoder-decoder architecture for improved lesion segmentation of covid-19 chest ct scans. *IEEE Transactions on Artificial Intelligence*, 2(3):283–297, 2021. 2
- [39] Najib J Majaj, Ha Hong, Ethan A Solomon, and James J DiCarlo. Simple learned weighted sums of inferior temporal neuronal firing rates accurately predict human core object recognition performance. *Journal of Neuroscience*, 35(39): 13402–13418, 2015. 4
- [40] Ran Margolin, Lihi Zelnik-Manor, and Ayellet Tal. How to evaluate foreground maps? In *Proceedings of the IEEE conference on computer vision and pattern recognition*, pages 248–255, 2014. 4
- [41] David Marr. *Vision: A computational investigation into the human representation and processing of visual information*. MIT press, 2010. 4
- [42] Teresa Mendonça, Pedro M Ferreira, Jorge S Marques, André RS Marcal, and Jorge Rozeira. Ph 2-a dermoscopic image database for research and benchmarking. In *2013 35th annual international conference of the IEEE engineer-*

- ing in medicine and biology society (EMBC), pages 5437–5440. IEEE, 2013. 6, 1, 5, 9
- [43] Fausto Milletari, Nassir Navab, and Seyed-Ahmad Ahmadi. V-net: Fully convolutional neural networks for volumetric medical image segmentation. In *2016 fourth international conference on 3D vision (3DV)*, pages 565–571. Ieee, 2016. 4
- [44] Ju-Hyeon Nam, Seo-Hyeong Park, Nur Suriza Syazwany, Yerim Jung, Yu-Han Im, and Sang-Chul Lee. M3fpolypsegnet: Segmentation network with multi-frequency feature fusion for polyp localization in colonoscopy images. In *2023 IEEE International Conference on Image Processing (ICIP)*, pages 1530–1534. IEEE, 2023. 2
- [45] Ju-Hyeon Nam, Nur Suriza Syazwany, Su Jung Kim, and Sang-Chul Lee. Modality-agnostic domain generalizable medical image segmentation by multi-frequency in multi-scale attention. In *Proceedings of the IEEE/CVF Conference on Computer Vision and Pattern Recognition*, pages 11480–11491, 2024. 5, 6, 8
- [46] Kenta Oono and Taiji Suzuki. Graph neural networks exponentially lose expressive power for node classification. In *International Conference on Learning Representations*, 2020. 4
- [47] Nobuyuki Otsu. A threshold selection method from gray-level histograms. *IEEE transactions on systems, man, and cybernetics*, 9(1):62–66, 1979. 2
- [48] Stephen E Palmer. *Vision science: Photons to phenomenology*. MIT press, 1999. 4
- [49] Michael I Posner, Steven E Petersen, et al. The attention system of the human brain. *Annual review of neuroscience*, 13(1):25–42, 1990. 4
- [50] Md Mostafijur Rahman and Radu Marculescu. G-cascade: Efficient cascaded graph convolutional decoding for 2d medical image segmentation. In *Proceedings of the IEEE/CVF Winter Conference on Applications of Computer Vision*, pages 7728–7737, 2024. 3, 5, 6, 8
- [51] Daniel Riccio, Nadia Brancati, Maria Frucci, and Diego Gragnaniello. A new unsupervised approach for segmenting and counting cells in high-throughput microscopy image sets. *IEEE journal of biomedical and health informatics*, 23(1):437–448, 2018. 2
- [52] Olaf Ronneberger, Philipp Fischer, and Thomas Brox. U-net: Convolutional networks for biomedical image segmentation. In *Medical Image Computing and Computer-Assisted Intervention–MICCAI 2015: 18th International Conference, Munich, Germany, October 5–9, 2015, Proceedings, Part III 18*, pages 234–241. Springer, 2015. 2, 5, 6, 8
- [53] Helena Shawn, Thompson Chyrikov, Jacob Lanet, Lam-chi Chen, Jim Zhao, and Christina Chajo. A ct image denoising method with residual encoder-decoder network. *arXiv preprint arXiv:2404.01553*, 2024. 2, 5
- [54] Juan Silva, Aymeric Histace, Olivier Romain, Xavier Dray, and Bertrand Granado. Toward embedded detection of polyps in wce images for early diagnosis of colorectal cancer. *International journal of computer assisted radiology and surgery*, 9:283–293, 2014. 6, 1, 8, 10
- [55] Abhishek Srivastava, Debesh Jha, Sukalpa Chanda, Umada Pal, Håvard D Johansen, Dag Johansen, Michael A Riegler, Sharib Ali, and Pål Halvorsen. Msrf-net: a multi-scale residual fusion network for biomedical image segmentation. *IEEE Journal of Biomedical and Health Informatics*, 26(5):2252–2263, 2021. 5, 6, 8
- [56] Nima Tajbakhsh, Suryakanth R Gurudu, and Jianming Liang. Automated polyp detection in colonoscopy videos using shape and context information. *IEEE transactions on medical imaging*, 35(2):630–644, 2015. 6, 1, 8, 10
- [57] Hamid R Tizhoosh. Image thresholding using type ii fuzzy sets. *Pattern recognition*, 38(12):2363–2372, 2005. 2
- [58] Athanasios Tragakis, Chaitanya Kaul, Roderick Murray-Smith, and Dirk Husmeier. The fully convolutional transformer for medical image segmentation. In *Proceedings of the IEEE/CVF Winter Conference on Applications of Computer Vision*, pages 3660–3669, 2023. 2
- [59] Stefan Treue. Neural correlates of attention in primate visual cortex. *Trends in neurosciences*, 24(5):295–300, 2001. 4
- [60] David Vázquez, Jorge Bernal, F Javier Sánchez, Gloria Fernández-Esparrach, Antonio M López, Adriana Romero, Michal Drozdal, Aaron Courville, et al. A benchmark for endoluminal scene segmentation of colonoscopy images. *Journal of healthcare engineering*, 2017, 2017. 6, 1, 8, 10
- [61] Tuan-Hung Vu, Himalaya Jain, Maxime Bucher, Matthieu Cord, and Patrick Pérez. Advent: Adversarial entropy minimization for domain adaptation in semantic segmentation. In *Proceedings of the IEEE/CVF conference on computer vision and pattern recognition*, pages 2517–2526, 2019. 5
- [62] Bin Wang, Hongyi Pan, Armstrong Aboah, Zheyuan Zhang, Elif Keles, Drew Torigian, Baris Turkbey, Elizabeth Krupinski, Jayaram Udupa, and Ulas Bagci. Gazegnn: A gaze-guided graph neural network for chest x-ray classification. In *Proceedings of the IEEE/CVF Winter Conference on Applications of Computer Vision*, pages 2194–2203, 2024. 3
- [63] Cheng Wang, Le Wang, Nuoqi Wang, Xiaoling Wei, Ting Feng, Minfeng Wu, Qi Yao, and Rongjun Zhang. Cfatransnet: Channel-wise cross fusion attention and transformer for 2d medical image segmentation. *Computers in Biology and Medicine*, 168:107803, 2024. 2, 5, 6, 8
- [64] Haonan Wang, Peng Cao, Jiaqi Wang, and Osmar R Zaiane. Uctransnet: rethinking the skip connections in u-net from a channel-wise perspective with transformer. In *Proceedings of the AAAI conference on artificial intelligence*, pages 2441–2449, 2022. 2
- [65] Qilong Wang, Banggu Wu, Pengfei Zhu, Peihua Li, Wangmeng Zuo, and Qinghua Hu. Eca-net: Efficient channel attention for deep convolutional neural networks. In *Proceedings of the IEEE/CVF conference on computer vision and pattern recognition*, pages 11534–11542, 2020. 4
- [66] Shujun Wang, Lequan Yu, Kang Li, Xin Yang, Chi-Wing Fu, and Pheng-Ann Heng. Boundary and entropy-driven adversarial learning for fundus image segmentation. In *Medical Image Computing and Computer Assisted Intervention–MICCAI 2019: 22nd International Conference, Shenzhen, China, October 13–17, 2019, Proceedings, Part I 22*, pages 102–110. Springer, 2019. 5

- [67] Wenhai Wang, Enze Xie, Xiang Li, Deng-Ping Fan, Kaitao Song, Ding Liang, Tong Lu, Ping Luo, and Ling Shao. Pvt v2: Improved baselines with pyramid vision transformer. *Computational Visual Media*, 8(3):415–424, 2022. 3
- [68] Yuan Wang, Kun Yu, Chen Chen, Xiyuan Hu, and Silong Peng. Dynamic graph learning with content-guided spatial-frequency relation reasoning for deepfake detection. In *Proceedings of the IEEE/CVF Conference on Computer Vision and Pattern Recognition*, pages 7278–7287, 2023. 3
- [69] Zhichao Wang, Lin Guo, Shuchang Zhao, Shiqing Zhang, Xiaoming Zhao, Jiangxiong Fang, Guoyu Wang, Hongsheng Lu, Jun Yu, and Qi Tian. Multi-scale group agent attention-based graph convolutional decoding networks for 2d medical image segmentation. *IEEE Journal of Biomedical and Health Informatics*, 2024. 3
- [70] Yu-Huan Wu, Yun Liu, Xin Zhan, and Ming-Ming Cheng. P2t: Pyramid pooling transformer for scene understanding. *IEEE transactions on pattern analysis and machine intelligence*, 2022. 3
- [71] Qing Xu, Zhicheng Ma, HE Na, and Wenting Duan. Dcsau-net: A deeper and more compact split-attention u-net for medical image segmentation. *Computers in Biology and Medicine*, 154:106626, 2023. 5, 6, 8
- [72] Shanshan Xu, Lianhong Duan, Yang Zhang, Zhicheng Zhang, Tiansheng Sun, and Lixia Tian. Graph-and transformer-guided boundary aware network for medical image segmentation. *Computer Methods and Programs in Biomedicine*, 242:107849, 2023. 3
- [73] Rex Ying, Ruining He, Kaifeng Chen, Pong Eksombatchai, William L Hamilton, and Jure Leskovec. Graph convolutional neural networks for web-scale recommender systems. In *Proceedings of the 24th ACM SIGKDD international conference on knowledge discovery & data mining*, pages 974–983, 2018. 3
- [74] Hang Zhang, Chongruo Wu, Zhongyue Zhang, Yi Zhu, Haibin Lin, Zhi Zhang, Yue Sun, Tong He, Jonas Mueller, R Manmatha, et al. Resnest: Split-attention networks. In *Proceedings of the IEEE/CVF conference on computer vision and pattern recognition*, pages 2736–2746, 2022. 3
- [75] Ju Zhang, Zhiyi Ye, Mingyang Chen, Jiahao Yu, and Yun Cheng. Transgraphnet: A novel network for medical image segmentation based on transformer and graph convolution. *Biomedical Signal Processing and Control*, 104: 107510, 2025. 3
- [76] Wenchao Zhang, Chong Fu, Yu Zheng, Fangyuan Zhang, Yanli Zhao, and Chiu-Wing Sham. Hsnet: A hybrid semantic network for polyp segmentation. *Computers in biology and medicine*, 150:106173, 2022. 3
- [77] Xiaoqi Zhao, Lihe Zhang, and Huchuan Lu. Automatic polyp segmentation via multi-scale subtraction network. In *Medical Image Computing and Computer Assisted Intervention—MICCAI 2021: 24th International Conference, Strasbourg, France, September 27–October 1, 2021, Proceedings, Part I 24*, pages 120–130. Springer, 2021. 2, 6
- [78] Xiaoqi Zhao, Hongpeng Jia, Youwei Pang, Long Lv, Feng Tian, Lihe Zhang, Weibing Sun, and Huchuan Lu. M²SNet: Multi-scale in multi-scale subtraction network for medical image segmentation. *arXiv preprint arXiv:2303.10894*, 2023. 2, 5, 6, 8
- [79] Zongwei Zhou, Md Mahfuzur Rahman Siddiquee, Nima Tajbakhsh, and Jianming Liang. Unet++: A nested u-net architecture for medical image segmentation. In *Deep Learning in Medical Image Analysis and Multimodal Learning for Clinical Decision Support: 4th International Workshop, DLMIA 2018, and 8th International Workshop, ML-CDS 2018, Held in Conjunction with MICCAI 2018, Granada, Spain, September 20, 2018, Proceedings 4*, pages 3–11. Springer, 2018. 2, 5, 6, 8
- [80] Zheming Zhuang, Nan Li, Alex Noel Joseph Raj, Vijayalakshmi GV Mahesh, and Shunmin Qiu. An rdau-net model for lesion segmentation in breast ultrasound images. *PLoS one*, 14(8):e0221535, 2019. 6, 1, 7, 9

TransGUNet: Transformer Meets Graph-based Skip Connection for Medical Image Segmentation

Supplementary Material

6. Dataset Descriptions

Segmentation Task	Dataset	Resolutions	Train	Test
Multi-organ Segmentation	Synapse	512×512	18 Scans	12 Scans
Skin Cancer Segmentation	ISIC2018	Variable	1868	261
COVID19 Infection Segmentation	COVID19-1	512×512	643	383
Breast Cancer Segmentation	BUSI	Variable	324	161
Polyp Segmentation	CVC-ClinicDB	384×288	490	62
	Kvasir-SEG	Variable	800	100

Table 6. Details of the medical segmentation *seen* clinical settings used in our experiments.

Segmentation Task	Dataset	Resolutions	Test
Multi-organ Segmentation	AMOS-CT	Variable	100 Scans
	AMOS-MRI	Variable	20 Scans
Skin Cancer Segmentation	PH2	767×576	200
COVID19 Infection Segmentation	COVID19-2	512×512	2535
Breast Cancer Segmentation	STU	Variable	42
Polyp Segmentation	CVC-300	574×500	60
	CVC-ColonDB	574×500	380
	ETIS	1255×966	196

Table 7. Details of the medical segmentation *unseen* clinical settings used in our experiments. Note that these datasets are used only for testing.

In this section, we describe the training and testing datasets used in this paper. Tab. 6 and Tab. 7 summarize the seen and unseen clinical setting datasets, respectively. We want to clarify that Tab. 7 datasets are used only to evaluate the generalizability of each model.

- *Multi-organ Segmentation:* The Synapse multi-organ segmentation dataset [3] is a widely recognized benchmark in the medical imaging community, specifically designed for the task of abdominal organ segmentation. The dataset consists of 30 abdominal CT scans, encompassing a total of 3,779 axial contrast-enhanced images. Each image is annotated by medical experts to identify and delineate eight different abdominal organs: the aorta, gallbladder, spleen, left kidney, right kidney, liver, pancreas, and stomach. The AMOS dataset [28] is an advanced and comprehensive benchmark dataset designed for the multi-organ segmentation. The dataset includes both Computed Tomography (CT) and Magnetic Resonance Imaging (MRI) scans, providing a diverse range of imaging data. We apply same preprocessing steps as the Synapse to ensure consistency. For evaluation, we separated into AMOS-CT (100 Scans) and AMOS-MRI (20 Scans), and the labels were aligned with those used in the Synapse. We want to clarify that AMOS-CT/MRI datasets are used only to evaluated the

generalizability of each model.

- *Breast Ultrasound Segmentation:* The BUSI dataset [2] comprises 780 images from 600 female patients, including 133 normal cases, 437 benign cases, and 210 malignant tumors. In contrast, the STU dataset [80] includes only 42 breast ultrasound images collected by Shantou University. Due to the limited number of images in the STU dataset, it is primarily used to evaluate the generalizability of models across different datasets.
- *Skin Lesion Segmentation:* The ISIC 2018 dataset [20] comprises 2,594 images of varying sizes. We randomly selected 1,868 images for training and 261 images for testing. Additionally, the PH2 dataset [42] was used to evaluate the domain generalizability of each model.
- *COVID19 Infection Segmentation:* The COVID19-1 dataset [30] contains 1,277 high-quality CT images. For our experiments, we randomly divided the dataset into 643 training images and 383 test images. To assess the domain generalizability of our models, we utilized the COVID19-2 dataset¹ solely for testing purposes.
- *Polyp Segmentation:* To train and evaluate our proposed model, we utilized five benchmark datasets: CVC-ColonDB [56], ETIS [54], Kvasir [27], CVC-300 [60], and CVC-ClinicDB [4]. For training, we adopted the same dataset as the latest image polyp segmentation method, comprising 800 samples from Kvasir and 490 samples from CVC-ClinicDB. The remaining images from these datasets, along with the other three datasets, were used exclusively for testing.

7. Intuitiveness and Design Principle of TransGUNet

We want to clarify that the design of TransGUNet is carefully considered rather than an ad-hoc decision, as follows: a) Medical images contain diverse anatomical structures, making it essential to flexibly capture both local details and global context. To address this, we transform cross-scale feature maps into a graph and apply efficient node-level attention. This design choice improves the model’s generalization across unseen clinical settings, as demonstrated in the “Ablation Study on ACS-GNN” section. b) Medical im-

¹<https://www.kaggle.com/datasets/piyushsamant11/pidata-new-names>

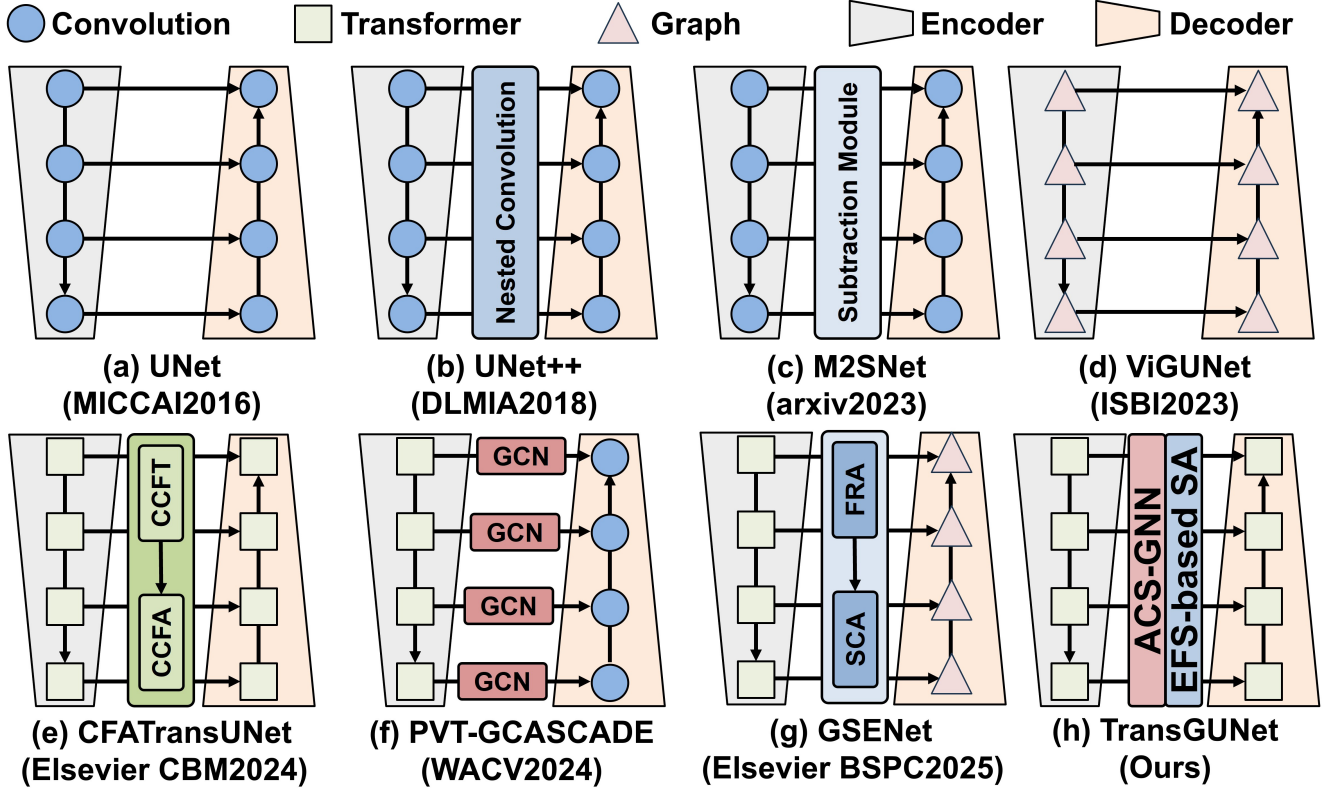


Figure 8. Comparison of skip connection frameworks scheme. Note that our unique approach (**TransGUNet**) incorporates *ACS-GNN* with *EFS-based spatial attention*.

ages segmentation models often produce uninformative feature maps (Figure 7 in the Appendix) due to various noise and irrelevant background artifacts, which can degrade the quality of spatial attention maps and reduce segmentation performance. To address this, we incorporate EFS-based spatial attention, prioritizing low-entropy feature maps to enhance the quality of spatial attention map. This novel approach also enhances generalization ability across unseen clinical settings, as shown in the "Ablation Study on EFS-based Attention" section.

8. Technical Novelty of TransGUNet

PVT-GCASCADe (WACV2024) vs TransGUNet. Like our approach, PVT-GCASCADe utilizes GNN; however, it does not consider cross-scale information, which is limited to medical images with more diverse lesion sizes. Additionally, unlike PVT-GCASCADe, it reduces the influence of uninformative feature maps with UFS to enable reliable spatial attention.

CFATransGNet (CBM2024) vs TransGUNet. TransGUNet focuses on efficiently reducing the semantic gap between the encoder and decoder using the GNN, which is not commonly used in skip connections. This suggests the

potential for further development of GNN-based skip connection engineering beyond Transformer-based skip connection engineering (CFATransUNet).

MADGNet (CVPR2024) vs TransGUNet. While MADGNet employs Multi-Frequency and Multi-Scale Attention mechanisms to enhance feature extraction, TransGUNet’s use of ACS-GNN allows for more robust integration of cross-scale features and adaptive learning of node importance. This novel approach not only improves segmentation accuracy but also addresses the limitations of traditional convolutional methods by leveraging the strengths of GNNs in handling diverse and noisy medical data.

9. Broader Impact in Artificial Intelligence

TransGUNet’s superior performance in medical image segmentation has the potential to reliable medical diagnostics and treatment planning. By providing accurate and reliable segmentation of complex anatomical structures, it enables healthcare professionals to make more informed decisions, leading to improved patient outcomes. The model’s effective integration of Graph Neural Networks (GNNs) and Transformer architectures demonstrates a hybrid approach that addresses the limitations of traditional convo-

Method	Parameters (M)	FLOPs (G)	Inference Time (ms)
UNet	8.2	23.7	10.1
UNet++	34.9	197.8	22.9
CENet	18.0	9.2	10.5
TransUNet	53.4	21.8	93.4
nnUNet	-	-	-
MSRFNet	21.5	156.6	73.8
DCSAUNet	25.9	9.2	24.3
M2SNet	25.3	12.8	32.1
ViGUNet	-	-	-
PVT-GCASCADe	25.4	7.9	17.4
CFATransUNet	64.6	32.9	36.0
MADGNet	29.8	16.8	24.0
TransGUNet (Ours)	25.0	10.0	19.4

Table 8. The number of parameters (M), FLOPs (G), and Inference Time (ms) of different models.

lutional neural networks (CNNs), enhancing robustness and adaptability across various AI tasks. Furthermore, TransGUNet highlights the importance of developing efficient AI models that do not compromise on performance. Techniques like entropy-driven feature selection (EFS) and attentional cross-scale GNNs optimize resource use, setting a new benchmark for efficiency in AI-driven medical applications. This balance between high performance and computational efficiency can guide future research in creating powerful and resource-conscious AI models.

10. More Detailed Ablation Study on TransGUNet

In this section, we perform a more detailed ablation study on TransGUNet.

10.1. Ablation Study on Backbone in TransGUNet

Network Type	Backbone	<i>Seen</i>		<i>Unseen</i>		Param (M)	FLOPs (G)
		DSC	mIoU	DSC	mIoU		
CNN	ResNet50	85.9	79.1	67.3	60.5	25.1M	18.0G
	Res2Net50	86.0	79.1	70.6	62.8	25.2M	18.8G
	ResNeSt50	86.6	79.7	73.3	64.9	26.9M	20.4G
Transformer	ViT-B-16	83.6	75.9	64.7	56.3	53.4M	18.4G
	PVT-v2-b2	86.6	80.0	77.0	68.3	26.3M	10.5G
	P2T-Small (Ours)	87.3	80.6	78.6	69.7	25.0M	10.0G

Table 9. Quantitative results for each *Seen* and *Unseen* datasets according to backbone network.

In this section, we conduct an ablation study to evaluate the impact of different backbone models on the performance of TransGUNet. This experiment uses several popular CNN and Transformer architectures, including ResNet50 [25], Res2Net [16], ResNeSt50 [74], ViT-B-16 [11], PVT-v2-b2 [67], and P2T-Small [70]. Notably, only the backbone network was changed, while all other architectural settings remained consistent with those in the main experiment. We reported the *mean* performance for each *seen* and *unseen* clinical settings in Tab. 9. The datasets used in the *seen* and *unseen* clinical settings are the same as Tab. 2 and Tab.

3, respectively. For convenience, we denote (\cdot, \cdot) as the performance improvement gap between TransGUNet and other models for seen and unseen clinical settings.

ResNeSt50, as utilized in MADGNet, achieves comparable or even superior performance. Furthermore, using PVT-v2-b2, as implemented in PVT-GCASCADe, yields higher performance in both seen and unseen clinical settings. Specifically, TransGUNet with PVT-v2-b2 outperforms PVT-GCASCADe by **(0.4%, 2.2%)** and **(0.7%, 2.2%)** in DSC and mIoU, respectively, demonstrating its robustness and effectiveness according to the backbone type.

10.2. Ablation Study on ECA Kernel Size in ACS-GNN

ECA Kernel Size k	<i>Seen</i>		<i>Unseen</i>		Param (M)	FLOPs (G)
	DSC	mIoU	DSC	mIoU		
$k = 3$ (Ours)	87.3	80.6	78.6	69.7	25.0M	10.0G
$k = 5$	87.5	80.7	78.3	69.6	25.0M	10.0G
$k = 7$	87.4	80.5	78.4	69.5	25.0M	10.0G

Table 10. Quantitative results for each *Seen* and *Unseen* datasets according to various ECA kernel size k .

In this section, we conduct an ablation study to compare the performance according to various ECA kernel size $k = \{3, 5, 7\}$. In the main manuscript, we used $k = 3$ as the ECA kernel size. We reported the *mean* performance for each *seen* and *unseen* clinical settings in Tab. 10. The datasets used in the *seen* and *unseen* clinical settings are the same as Tab. 2 and Tab. 3, respectively.

As listed in Tab. 10, we observed that while increasing the kernel size for $k = 3$ to $k = 7$, it does not provide meaningful statistical improvement. Consequently, we choose $k = 3$ as our model basic configuration in ECA kernel size.

10.3. Ablation Study on Repetition Time of ACS-GNN with EFS-based Spatial Attention

Repetition Time G	<i>Seen</i>		<i>Unseen</i>		Param (M)	FLOPs (G)
	DSC	mIoU	DSC	mIoU		
$G = 3$	86.7	80.0	77.4	68.6	26.6M	12.4G
$G = 5$	86.4	79.7	77.2	68.3	28.1M	14.7G
$G = 7$	86.3	80.0	77.1	68.3	29.6M	17.0G
$G = 9$	86.3	79.7	77.1	68.2	31.1M	19.4G
$G = 1$ (Ours)	87.3	80.6	78.6	69.7	25.0M	10.0G

Table 11. Quantitative results for each *Seen* and *Unseen* datasets according to repetition time G of ACS-GNN with EFS-based spatial attention.

In this section, we conduct an ablation study to compare the performance according to repetition time $G \in \{1, 3, 5, 7, 9\}$ of ACS-GNN with EFS-based spatial attention. In the main manuscript, we used $G = 1$ as the default repetition time. We reported the *mean* performance for each *seen* and *unseen* clinical settings in Tab. 11. The datasets

used in the *seen* and *unseen* clinical settings are the same as Tab. 2 and Tab. 3, respectively.

The ablation study reveals that repeating the ACS-GNN module with EFS-based spatial attention leads to overfitting. Despite the increased capacity of the model, performance decreased on both seen and unseen datasets. This result indicates that the model is overfitting to the training data.

11. Metrics Descriptions

In this section, we describe the metrics used in this paper. For convenience, we denote TP , FP , and FN as the number of samples of true positive, false positive, and false negative between two binary masks A and B .

- The *Mean Dice Similarity Coefficient (DSC)* [43] measures the similarity between two samples and is widely used to assess the performance of segmentation tasks, such as image segmentation or object detection. **Higher is better.** For given two binary masks A and B , DSC is defined as follows:

$$\text{DSC}(A, B) = \frac{2 \times |A \cap B|}{|A \cup B|} = \frac{2 \times TP}{2 \times TP + FP + FN} \quad (8)$$

- The *Mean Intersection over Union (mIoU)* measures the ratio of the intersection area to the union area between predicted and ground truth masks in segmentation tasks. **Higher is better.** For given two binary masks A and B , mIoU is defined as follows:

$$\text{mIoU}(A, B) = \frac{A \cap B}{A \cup B} = \frac{TP}{TP + FP + FN} \quad (9)$$

- The *Mean Weighted F-Measure F_β^ω* [40] is a metric that combines weighted precision $Precision^\omega$ (Measure of exactness) and weighted recall $Recall^\omega$ (Measure of completeness) into a single value by calculating the harmonic mean. β signifies the effectiveness of detection with respect to a user who attaches β times as much importance to $Recall^\omega$ as to $Precision^\omega$. **Higher is better.** F_β^ω is defined as follows:

$$F_\beta^\omega = (1 + \beta^2) \cdot \frac{Precision^\omega \cdot Recall^\omega}{\beta^2 \cdot Precision^\omega + Recall^\omega} \quad (10)$$

- The *Mean S-Measure S_α* [13] is used to evaluate the quality of image segmentation, specifically focusing on the structural similarity between the region-aware S_o and object-aware S_r . **Higher is better.** S_α is defined as follows:

$$S_\alpha = \gamma S_o + (1 - \gamma) S_r \quad (11)$$

- *Mean E-Measure E_ϕ^{max}* [14] assesses the edge accuracy in edge detection or segmentation tasks. It evaluates how well the predicted edges align with the ground truth

edges using foreground map FM . **Higher is better.** E_ϕ^{max} is defined as follows:

$$E_\phi^{max} = \frac{1}{H \times W} \sum_{h=1}^H \sum_{w=1}^W \phi FM(h, w) \quad (12)$$

- *Mean Absolute Error (MAE)* calculates the average absolute differences between predicted and ground truth values. **Lower is better.** For given two binary masks A and B , MAE is defined as follows:

$$\text{MAE}(A, B) = \frac{1}{H \times W} \sum_{h=1}^H \sum_{w=1}^W |A(h, w) - B(h, w)| \quad (13)$$

- *Hausdorff Distance 95 (HD95)* [6] is the 95th percentile of the Hausdorff Distance, which means it excludes the top 5% of the most extreme distances for more robust to noise and outliers. It is calculated by first computing all pairwise distances between the points in the predicted and ground truth segmentations, sorting these distances, and then taking the 95th percentile value. Note that the Hausdorff distance ranges from 0, indicating no difference when two sets are identical, to infinity, as the maximum distance between two sets can grow indefinitely. **Lower is better.** For given two binary masks A and B and euclidean distance $d(\cdot, \cdot)$, HD is defined as follows:

$$\begin{aligned} \text{HD}(A, B) \\ = \max(\max_{a \in A} \min_{b \in B} d(a, b), \max_{b \in B} \min_{a \in A} d(a, b)) \end{aligned} \quad (14)$$

12. More Qualitative and Quantitative Results

In this section, we provide the quantitative results with various metrics in Tab. 12, 13, 14, 15 for binary segmentation. Additionally, we also provide the quantitative results in Tab. 16, 17, 18 with each organ for multi-organ segmentation. For all tables, **Bold** and *italic* are the first and second best performance results, respectively. We also present more various qualitative results on datasets in Fig. 9, 10, 11, 12.

Skin Lesion Segmentation

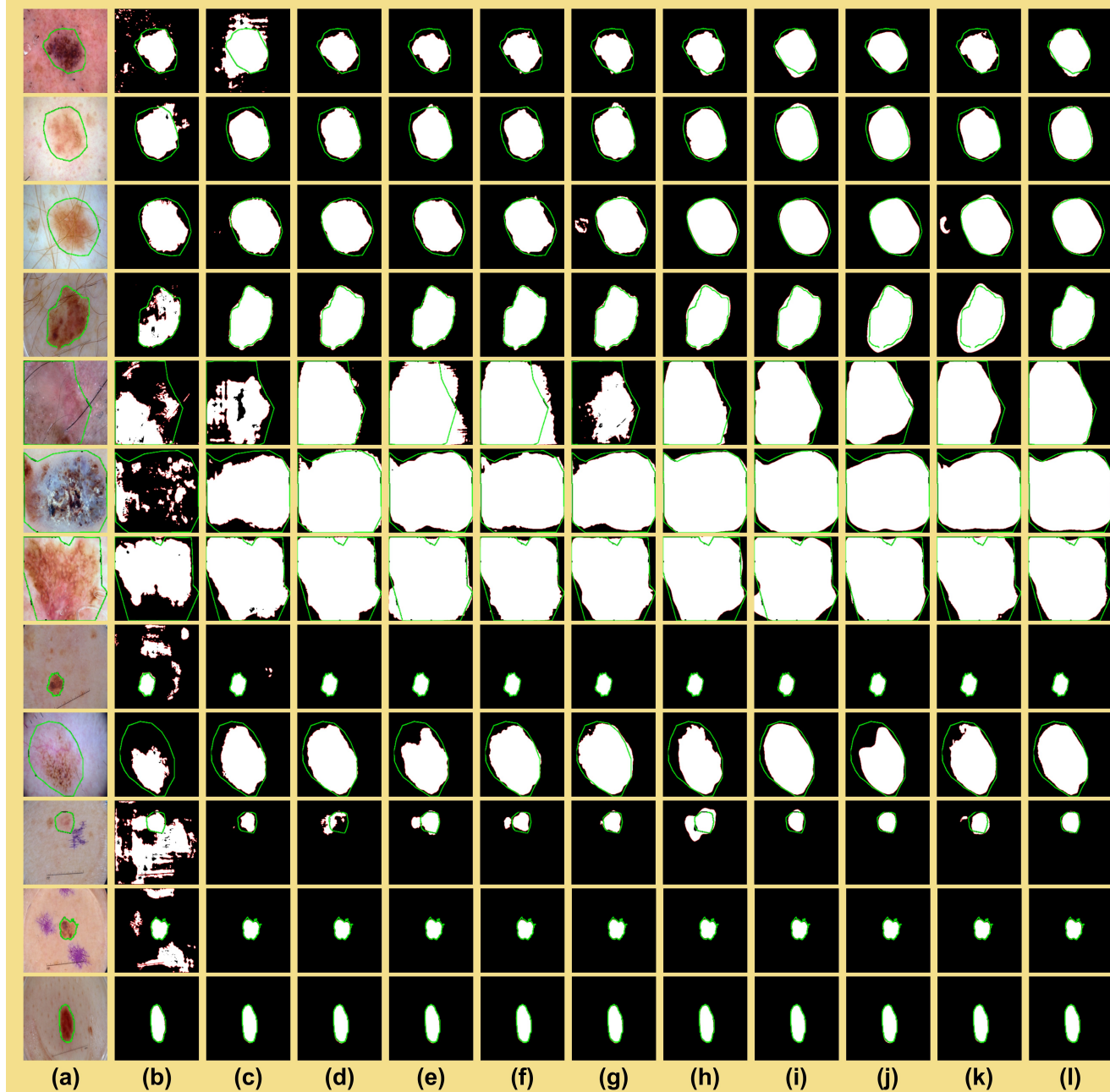


Figure 9. Qualitative comparison of other methods and **TransGUNet** on **Skin Lesion Segmentation** [20, 42]. (a) Input images with ground truth. (b) UNet. (c) UNet++. (d) CENet. (e) TransUNet. (f) MSRFNet. (g) DCSAUNet. (h) M2SNet. (i) PVT-GCASCADE. (j) CFATransUNet. (k) MADGNet. (l) **TransGUNet (Ours)**. **Green** and **Red** lines denote the boundaries of the ground truth and prediction, respectively.

COVID19 Infection Segmentation

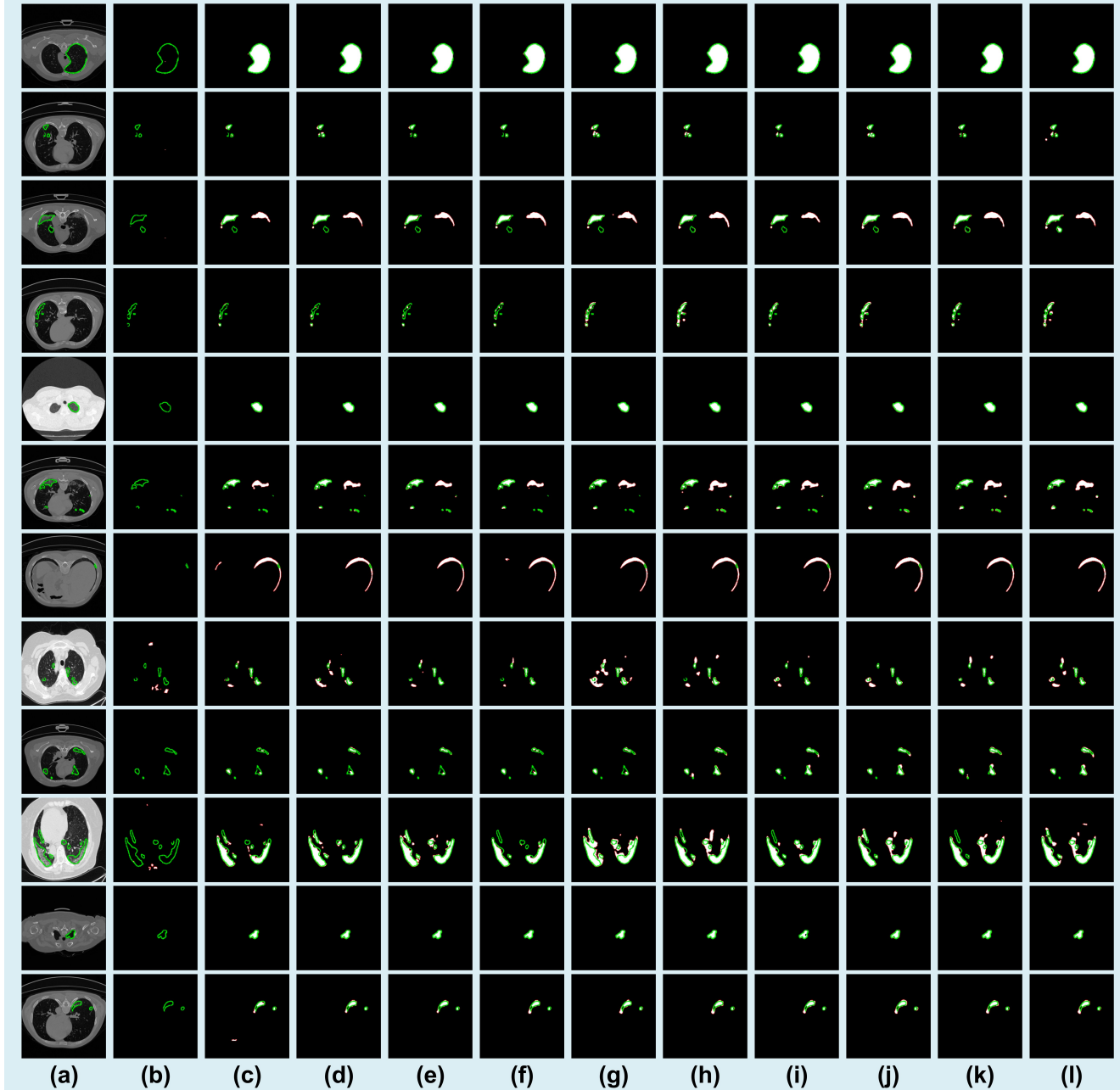


Figure 10. Qualitative comparison of other methods and **TransGUNet** on **COVID19 Infection Segmentation** [30]. (a) Input images with ground truth. (b) UNet. (c) UNet++. (d) CENet. (e) TransUNet. (f) MSRFNet. (g) DCSAUNet. (h) M2SNet. (i) PVT-GCASCADE. (j) CFATransUNet. (k) MADGNet. (l) **TransGUNet (Ours)**. **Green** and **Red** lines denote the boundaries of the ground truth and prediction, respectively.

Breast Tumor Segmentation

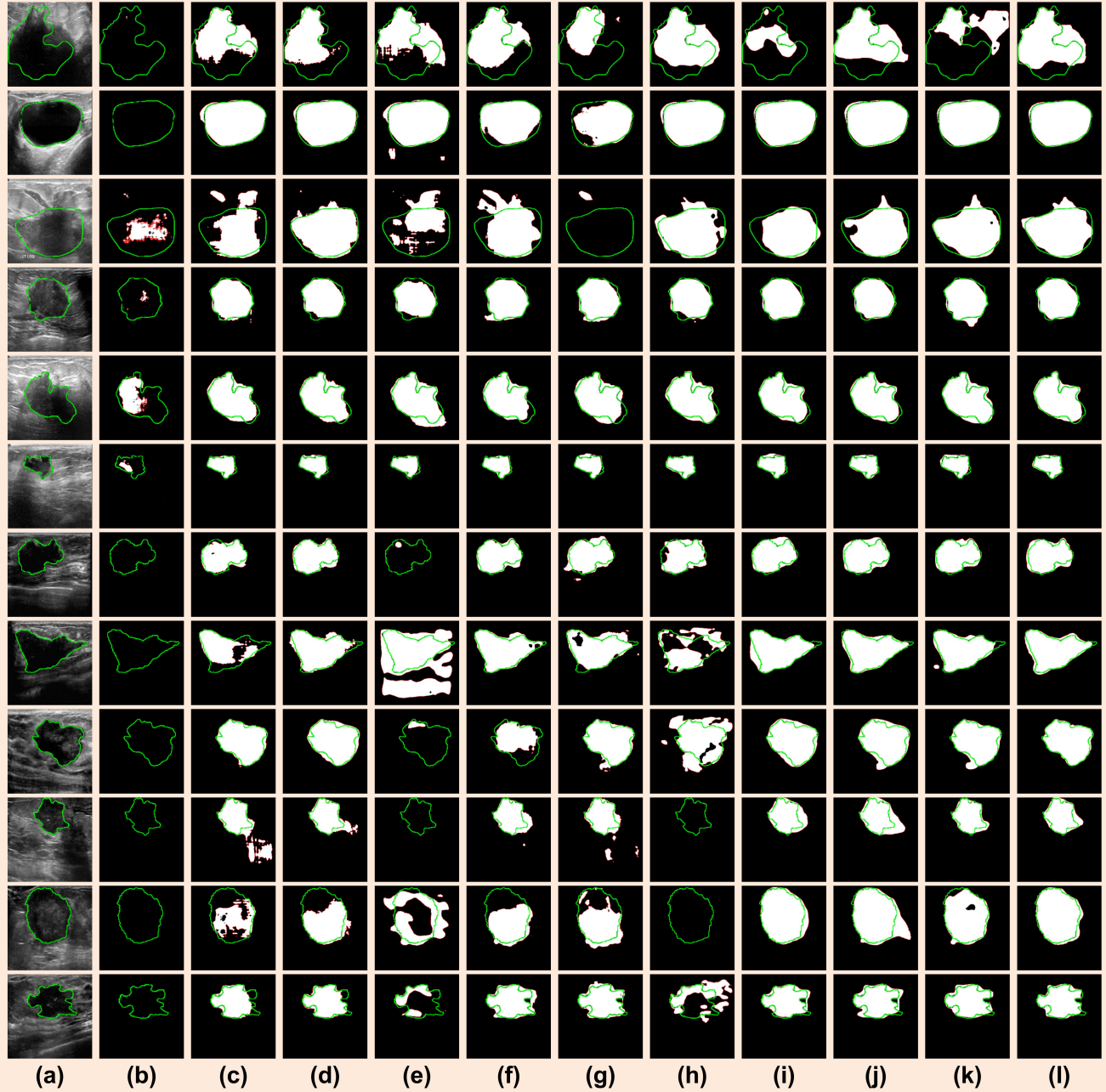


Figure 11. Qualitative comparison of other methods and **TransGUNet** on **Breast Tumor Segmentation** [2, 80]. (a) Input images with ground truth. (b) UNet. (c) UNet++. (d) CENet. (e) TransUNet. (f) MSRFNet. (g) DCSAUNet. (h) M2SNet. (i) PVT-GCASCADE. (j) CFATransUNet. (k) MADGNet. (l) **TransGUNet (Ours)**. Green and Red lines denote the boundaries of the ground truth and prediction, respectively.

Polyp Segmentation

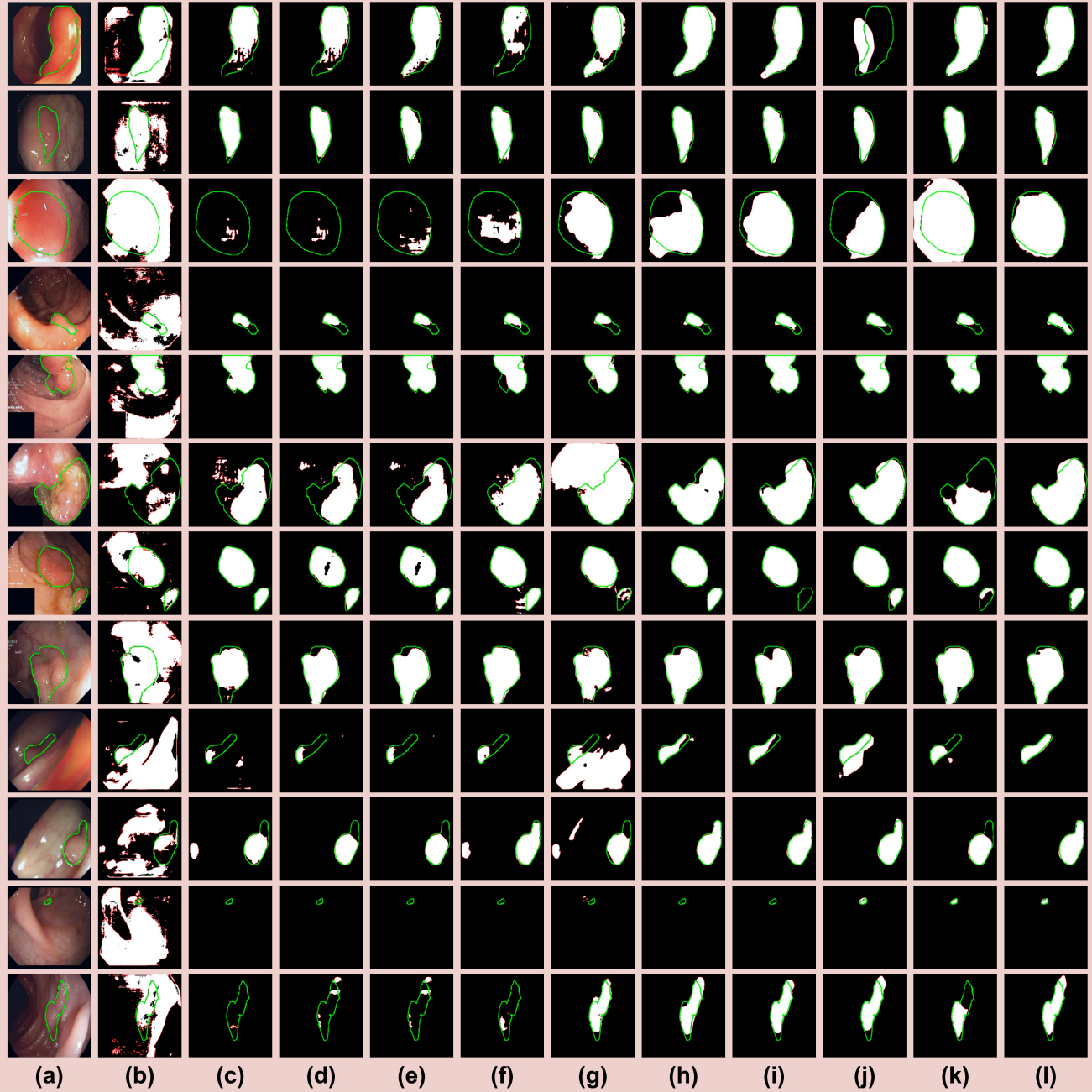


Figure 12. Qualitative comparison of other methods and **TransGUNet** on **Polyp Segmentation** [4, 27, 54, 56, 60]. (a) Input images with ground truth. (b) UNet. (c) UNet++. (d) CENet. (e) TransUNet. (f) MSRFNet. (g) DCSAUNet. (h) M2SNet. (i) PVT-GCASCADE. (j) CFATransUNet. (k) MADGNet. (l) **TransGUNet (Ours)**. Green and Red lines denote the boundaries of the ground truth and prediction, respectively.

Method	ISIC2018 \Rightarrow ISIC2018					
	DSC \uparrow	mIoU \uparrow	$F_{\beta}^{w} \uparrow$	$S_{\alpha} \uparrow$	$E_{\phi}^{max} \uparrow$	MAE \downarrow
UNet (MICCAI2016)	86.9	80.2	87.9	80.4	91.3	4.7
UNet++ (DLMIA2018)	87.8	80.5	86.5	80.5	92.0	4.5
CENet (TMI2019)	89.1	82.1	88.1	81.3	93.0	4.3
TransUNet (arxiv2021)	87.3	81.2	88.6	80.8	91.9	4.2
MSRFNet (BHI2022)	88.2	81.3	86.9	80.7	92.0	4.7
DCSAUNet (CBM2023)	89.0	82.0	87.8	81.4	92.9	4.4
M2SNet (arxiv2023)	89.2	83.4	90.0	82.0	93.8	3.7
PVT-GCASCADe (WACV2024)	90.3	83.5	88.9	82.0	93.9	3.7
CFATransUNet (CBM2024)	90.1	83.5	89.0	82.1	94.1	3.5
MADGNet (CVPR2024)	90.2	83.7	89.2	82.0	94.1	3.6
TransGUNet (Ours)	91.1	84.8	90.1	82.6	94.4	3.4
	+0.8	+1.1	+0.1	+0.5	+0.3	+0.2
Method	ISIC2018 \Rightarrow PH2					
	DSC \uparrow	mIoU \uparrow	$F_{\beta}^{w} \uparrow$	$S_{\alpha} \uparrow$	$E_{\phi}^{max} \uparrow$	MAE \downarrow
UNet (MICCAI2016)	90.3	83.5	88.4	74.8	90.8	6.9
UNet++ (DLMIA2018)	88.0	80.1	85.7	73.2	89.2	7.9
CENet (TMI2019)	90.5	83.3	87.3	78.1	91.5	6.0
TransUNet (arxiv2021)	89.5	82.1	86.9	74.3	90.3	6.7
MSRFNet (BHI2022)	90.5	83.5	87.5	75.0	91.4	6.0
DCSAUNet (CBM2023)	89.0	81.5	85.7	74.0	90.2	6.9
M2SNet (arxiv2023)	90.7	83.5	87.6	75.5	92.0	5.9
PVT-GCASCADe (WACV2024)	91.5	84.9	88.6	76.3	92.7	5.3
CFATransUNet (CBM2024)	91.5	85.0	88.7	76.3	92.6	5.3
MADGNet (CVPR2024)	91.3	84.6	88.4	76.2	92.8	5.1
TransGUNet (Ours)	91.7	85.2	88.9	76.6	93.1	5.0
	+0.2	+0.2	+0.2	-1.5	+0.3	+0.1

Table 12. Segmentation results on **Skin Lesion Segmentation**. We train each model on ISIC2018 [20] train dataset and evaluate on ISIC2018 [20] and PH2 [42] test datasets.

Method	COVID19-1 \Rightarrow COVID19-1					
	DSC \uparrow	mIoU \uparrow	$F_{\beta}^{w} \uparrow$	$S_{\alpha} \uparrow$	$E_{\phi}^{max} \uparrow$	MAE \downarrow
UNet (MICCAI2016)	47.7	38.6	36.1	69.6	62.7	2.1
UNet++ (DLMIA2018)	65.6	57.1	54.4	78.8	73.2	1.3
CENet (TMI2019)	76.3	69.2	64.4	83.2	76.6	0.6
TransUNet (arxiv2021)	75.6	68.8	63.4	82.7	75.5	0.7
MSRFNet (BHI2022)	75.2	68.0	63.4	82.7	76.3	0.8
DCSAUNet (CBM2023)	75.3	68.2	63.1	83.0	77.3	0.7
M2SNet (arxiv2023)	81.7	74.7	68.3	85.7	80.1	0.6
PVT-GCASCADe (WACV2024)	82.3	74.8	68.1	85.8	80.1	0.5
CFATransUNet (CBM2024)	80.4	73.6	68.3	84.8	79.2	0.5
MADGNet (CVPR2024)	83.7	76.8	70.2	86.3	81.5	0.5
TransGUNet (Ours)	84.0	77.0	70.2	86.6	81.2	0.4
	+0.3	+0.2	+0.0	+0.3	-0.3	+0.1
Method	COVID19-1 \Rightarrow COVID19-2					
	DSC \uparrow	mIoU \uparrow	$F_{\beta}^{w} \uparrow$	$S_{\alpha} \uparrow$	$E_{\phi}^{max} \uparrow$	MAE \downarrow
UNet (MICCAI2016)	47.1	37.7	46.7	68.7	68.6	1.0
UNet++ (DLMIA2018)	50.5	40.9	50.6	69.8	75.7	1.0
CENet (TMI2019)	60.1	49.9	61.1	73.4	80.1	1.1
TransUNet (arxiv2021)	56.9	48.0	58.0	72.5	79.7	0.8
MSRFNet (BHI2022)	58.3	48.4	59.1	72.7	79.8	1.0
DCSAUNet (CBM2023)	52.4	44.0	52.0	71.3	76.3	1.0
M2SNet (arxiv2023)	68.6	58.9	68.5	76.9	86.1	1.1
PVT-GCASCADe (WACV2024)	71.0	60.4	70.0	77.8	87.9	1.2
CFATransUNet (CBM2024)	65.7	56.2	67.0	75.1	83.0	1.2
MADGNet (CVPR2024)	72.2	62.6	72.3	78.2	88.1	1.0
TransGUNet (Ours)	73.0	62.4	72.0	78.7	89.5	0.9
	+0.8	-0.2	-0.3	+0.5	+1.4	-0.1

Table 13. Segmentation results on **COVID19 Infection Segmentation**. We train each model on COVID19-1 [30] train dataset and evaluate on COVID19-1 [30] and COVID19-2 test datasets.

Method	BUSI \Rightarrow BUSI					
	DSC \uparrow	mIoU \uparrow	$F_{\beta}^{w} \uparrow$	$S_{\alpha} \uparrow$	$E_{\phi}^{max} \uparrow$	MAE \downarrow
UNet (MICCAI2016)	69.5	60.2	67.2	76.9	83.2	4.8
UNet++ (DLMIA2018)	71.3	62.3	68.9	78.1	84.4	4.8
CENet (TMI2019)	79.7	71.5	78.1	82.8	91.1	3.9
TransUNet (arxiv2021)	75.5	68.4	73.8	79.8	88.6	4.2
MSRFNet (BHI2022)	76.6	68.1	75.1	80.9	88.5	4.2
DCSAUNet (CBM2023)	73.7	65.0	71.5	79.6	86.0	4.6
M2SNet (arxiv2023)	80.4	72.5	78.7	83.0	91.2	4.1
PVT-GCASCADe (WACV2024)	82.0	73.6	80.2	83.7	92.1	3.8
CFATransUNet (CBM2024)	80.6	72.8	79.5	83.1	91.1	4.1
MADGNet (CVPR2024)	81.3	73.4	79.5	83.8	91.7	3.6
TransGUNet (Ours)	82.7	74.7	81.0	84.3	93.0	3.7
	+1.0	+1.1	+0.8	+0.5	+0.9	-0.1
Method	BUSI \Rightarrow STU					
	DSC \uparrow	mIoU \uparrow	$F_{\beta}^{w} \uparrow$	$S_{\alpha} \uparrow$	$E_{\phi}^{max} \uparrow$	MAE \downarrow
UNet (MICCAI2016)	71.6	61.6	71.6	76.1	82.4	5.2
UNet++ (DLMIA2018)	77.0	68.0	76.3	79.8	86.7	4.4
CENet (TMI2019)	86.0	77.2	84.2	84.5	93.7	2.8
TransUNet (arxiv2021)	41.4	32.1	40.8	60.2	58.1	9.7
MSRFNet (BHI2022)	84.0	75.2	75.1	83.5	92.2	3.1
DCSAUNet (CBM2023)	86.1	76.5	82.7	84.9	94.7	3.2
M2SNet (arxiv2023)	79.4	69.3	76.4	81.3	90.7	4.3
PVT-GCASCADe (WACV2024)	86.4	76.6	82.2	84.3	84.2	3.1
CFATransUNet (CBM2024)	87.9	79.2	85.3	85.7	95.4	2.6
MADGNet (CVPR2024)	88.4	79.9	86.4	86.2	95.9	2.6
TransGUNet (Ours)	87.4	78.2	84.1	85.4	94.9	2.7
	-1.0	-1.7	-2.3	-0.8	-1.0	-0.1

Table 14. Segmentation results on **Breast Tumor Segmentation**. We train each model on BUSI [2] train dataset and evaluate on BUSI [2] and STU [80] test datasets.

Method	CVC-ClinicDB + Kvasir-SEG \Rightarrow CVC-ClinicDB					
	DSC \uparrow	mIoU \uparrow	F_{β}^w \uparrow	S_{α} \uparrow	E_{ϕ}^{max} \uparrow	MAE \downarrow
UNet (MICCAI2016)	76.5	69.1	75.1	83.0	86.4	2.7
UNet++ (DLMIA2018)	79.7	73.6	79.4	85.1	88.3	2.2
CENet (TMI2019)	89.4	84.0	89.1	89.8	96.0	1.1
TransUNet (arxiv2021)	87.4	82.4	87.2	88.5	95.2	1.3
MSRFNet (BHI2022)	83.2	76.5	81.9	86.4	91.3	1.7
DCSAUNet (CBM2023)	80.6	73.7	79.6	84.9	89.9	2.4
M2SNet (arxiv2023)	92.8	88.2	92.3	91.4	97.7	0.7
PVT-GCASCADe (WACV2024)	92.2	87.6	91.6	91.8	97.0	0.8
CFATransUNet (CBM2024)	91.0	86.2	90.8	90.7	97.0	0.8
MADGNet (CVPR2024)	93.9	89.5	93.6	92.2	98.5	0.7
TransGUNet (Ours)	92.3	87.7	91.8	91.6	97.1	0.7
	-1.6	-1.8	-1.8	-0.6	-1.4	+0.0
Method	CVC-ClinicDB + Kvasir-SEG \Rightarrow Kvasir-SEG					
	DSC \uparrow	mIoU \uparrow	F_{β}^w \uparrow	S_{α} \uparrow	E_{ϕ}^{max} \uparrow	MAE \downarrow
UNet (MICCAI2016)	80.5	72.6	78.2	79.9	88.2	5.2
UNet++ (DLMIA2018)	84.3	77.4	83.1	82.1	90.5	4.6
CENet (TMI2019)	89.5	83.9	88.9	85.3	94.1	3.0
TransUNet (arxiv2021)	86.4	80.1	85.4	83.0	92.1	4.0
MSRFNet (BHI2022)	86.1	79.3	84.9	82.8	92.0	4.0
DCSAUNet (CBM2023)	82.6	75.2	80.7	81.3	90.1	4.9
M2SNet (arxiv2023)	90.2	85.1	89.4	85.6	94.6	2.7
PVT-GCASCADe (WACV2024)	91.6	86.8	91.0	86.4	96.3	2.4
CFATransUNet (CBM2024)	92.1	87.2	91.7	86.6	96.0	2.2
MADGNet (CVPR2024)	90.7	85.3	89.9	85.6	94.7	3.1
TransGUNet (Ours)	93.1	88.4	92.6	87.1	96.6	2.0
	+1.0	+1.2	+0.9	+0.5	+0.3	-0.2
Method	CVC-ClinicDB + Kvasir-SEG \Rightarrow CVC-300					
	DSC \uparrow	mIoU \uparrow	F_{β}^w \uparrow	S_{α} \uparrow	E_{ϕ}^{max} \uparrow	MAE \downarrow
UNet (MICCAI2016)	66.1	58.5	65.0	79.7	80.0	1.7
UNet++ (DLMIA2018)	64.4	58.4	63.7	79.5	77.4	1.8
CENet (TMI2019)	85.4	78.2	84.2	90.2	94.0	0.8
TransUNet (arxiv2021)	85.0	77.3	83.1	89.4	95.2	1.1
MSRFNet (BHI2022)	72.3	65.4	71.2	83.5	84.6	1.4
DCSAUNet (CBM2023)	68.9	59.8	66.3	81.1	83.8	2.0
M2SNet (arxiv2023)	89.8	83.2	88.3	93.0	97.0	0.6
PVT-GCASCADe (WACV2024)	88.2	81.0	85.9	92.0	95.6	0.9
CFATransUNet (CBM2024)	89.1	82.4	87.4	92.5	96.6	0.7
MADGNet (CVPR2024)	87.4	79.9	84.5	92.0	94.7	0.9
TransGUNet (Ours)	90.0	83.1	88.0	93.2	96.8	0.7
	+0.2	-0.1	-0.3	+0.2	+0.2	-0.1
Method	CVC-ClinicDB + Kvasir-SEG \Rightarrow CVC-ColonDB					
	DSC \uparrow	mIoU \uparrow	F_{β}^w \uparrow	S_{α} \uparrow	E_{ϕ}^{max} \uparrow	MAE \downarrow
UNet (MICCAI2016)	56.8	49.0	55.9	72.6	73.9	5.1
UNet++ (DLMIA2018)	57.5	50.2	56.6	73.3	73.9	5.0
CENet (TMI2019)	65.9	59.2	65.8	77.7	79.5	4.0
TransUNet (arxiv2021)	63.7	58.4	62.8	75.8	79.3	4.8
MSRFNet (BHI2022)	61.5	54.8	60.8	75.4	76.1	4.5
DCSAUNet (CBM2023)	57.8	49.3	54.9	73.3	76.0	5.8
M2SNet (arxiv2023)	75.8	68.5	73.7	84.2	86.9	3.8
PVT-GCASCADe (WACV2024)	79.5	71.6	77.7	84.5	89.6	3.8
CFATransUNet (CBM2024)	78.0	70.3	77.3	83.7	88.7	3.5
MADGNet (CVPR2024)	77.5	69.7	76.2	83.3	88.0	3.2
TransGUNet (Ours)	82.0	74.1	80.5	85.6	92.0	3.0
	+2.5	+2.5	+2.8	+1.1	+2.4	+0.2
Method	CVC-ClinicDB + Kvasir-SEG \Rightarrow ETIS					
	DSC \uparrow	mIoU \uparrow	F_{β}^w \uparrow	S_{α} \uparrow	E_{ϕ}^{max} \uparrow	MAE \downarrow
UNet (MICCAI2016)	41.6	35.4	39.5	67.2	61.7	2.7
UNet++ (DLMIA2018)	39.1	34.0	38.3	65.8	59.3	2.7
CENet (TMI2019)	57.0	51.4	56.0	74.9	73.8	2.2
TransUNet (arxiv2021)	50.1	44.0	48.8	70.7	68.7	2.6
MSRFNet (BHI2022)	38.3	33.7	36.9	66.0	58.4	3.6
DCSAUNet (CBM2023)	43.0	36.1	40.5	67.9	69.3	4.1
M2SNet (arxiv2023)	74.9	67.8	71.2	84.6	87.2	1.7
PVT-GCASCADe (WACV2024)	79.5	71.6	76.6	86.3	90.0	1.7
CFATransUNet (CBM2024)	77.0	69.5	75.0	84.4	88.6	1.5
MADGNet (CVPR2024)	77.0	69.7	75.3	84.6	88.4	1.6
TransGUNet (Ours)	81.3	73.1	76.8	87.6	91.5	1.4
	+1.8	+1.5	+0.2	+1.3	+1.5	+0.1

Table 15. Segmentation results on **Polyp Segmentation**. We train each model on CVC-ClinicDB [4] + Kvasir-SEG [27] train dataset and evaluate on CVC-ClinicDB [4], Kvasir-SEG [27], CVC-300 [60], CVC-ColonDB [56], and ETIS [54] test datasets.

Method	Synapse \Rightarrow Synapse								
	Average	Aorta	Gallbladder	Left Kidney	Right Kidney	Liver	Pancreas	Spleen	Stomach
UNet (MICCAI2016)	69.8	84.3	44.1	73.0	71.9	91.8	46.0	79.2	68.0
UNet++ (DLMIA2018)	79.3	87.4	64.8	81.2	77.9	94.3	60.8	89.6	78.7
CENet (TMI2019)	75.2	81.3	55.1	80.3	77.1	94.0	47.8	87.2	78.4
TransUNet (arxiv2021)	77.5	87.2	63.1	81.9	77.0	94.1	55.9	85.1	75.6
MSRFNet (BHI2022)	77.2	87.6	58.3	82.8	73.6	94.6	57.3	88.3	75.4
DCSAUNet (CBM2023)	71.0	81.4	51.9	75.1	68.8	92.7	45.4	84.6	68.0
M2SNet (arxiv2023)	77.1	84.9	55.6	78.2	76.1	94.9	57.4	89.1	80.3
PVT-GCASCADe (WACV2024)	78.1	85.1	57.0	82.2	79.3	94.9	55.2	88.7	82.7
CFATransUNet (CBM2024)	80.5	85.8	65.9	85.8	81.7	95.2	59.4	89.0	81.4
MADGNet (CVPR2024)	79.3	85.2	59.9	85.4	78.0	94.5	60.5	88.2	83.0
TransGUNet (Ours)	80.9	86.6	61.0	87.0	83.8	95.3	59.7	89.4	84.6
	+0.4	-0.6	-4.9	+1.2	+2.1	+0.1	-0.8	-0.2	+1.6
Method	Synapse \Rightarrow AMOS-CT								
	Average	Aorta	Gallbladder	Left Kidney	Right Kidney	Liver	Pancreas	Spleen	Stomach
UNet (MICCAI2016)	56.3	62.8	43.2	50.3	55.3	84.6	26.8	68.9	58.8
UNet++ (DLMIA2018)	67.5	67.0	62.7	65.2	65.9	88.2	42.3	78.1	70.4
CENet (TMI2019)	67.9	72.4	52.0	69.5	72.3	89.3	40.8	78.9	68.2
TransUNet (arxiv2021)	68.3	75.4	60.4	65.3	68.5	90.3	38.2	78.6	69.8
MSRFNet (BHI2022)	61.8	70.7	54.1	57.8	54.6	87.4	31.7	75.8	62.1
DCSAUNet (CBM2023)	45.7	43.4	30.6	32.5	39.5	85.1	18.7	67.6	48.0
M2SNet (arxiv2023)	69.6	74.4	60.9	66.7	69.5	90.8	41.8	79.6	73.3
PVT-GCASCADe (WACV2024)	69.3	70.5	56.6	64.6	71.9	91.7	42.0	82.0	75.4
CFATransUNet (CBM2024)	68.0	75.0	51.8	67.5	74.5	88.2	43.6	78.2	65.5
MADGNet (CVPR2024)	74.9	79.4	63.3	77.6	75.6	90.7	51.9	83.2	77.3
TransGUNet (Ours)	76.5	81.0	63.4	79.1	82.3	91.9	57.4	84.7	78.3
	+1.6	+1.6	+0.1	+1.5	+6.7	+0.2	-0.5	+1.5	+1.0
Method	Synapse \Rightarrow AMOS-MRI								
	Average	Aorta	Gallbladder	Left Kidney	Right Kidney	Liver	Pancreas	Spleen	Stomach
UNet (MICCAI2016)	8.3	6.1	5.6	3.0	14.0	26.1	1.2	4.9	5.1
UNet++ (DLMIA2018)	6.0	9.7	6.7	7.9	2.7	7.1	1.5	4.6	7.6
CENet (TMI2019)	14.5	13.4	6.2	21.8	34.7	14.6	5.7	9.5	9.8
TransUNet (arxiv2021)	9.1	10.2	8.0	18.9	21.1	7.5	1.9	2.7	2.8
MSRFNet (BHI2022)	6.5	2.6	6.9	3.7	3.0	26.9	1.4	2.4	4.9
DCSAUNet (CBM2023)	1.7	0.9	1.7	0.0	0.8	7.8	0.0	1.8	0.4
M2SNet (arxiv2023)	22.0	29.1	8.4	35.0	34.5	29.0	5.1	18.5	16.7
PVT-GCASCADe (WACV2024)	32.8	26.8	11.6	44.1	47.8	64.3	3.9	38.3	25.5
CFATransUNet (CBM2024)	35.8	30.0	16.9	41.8	47.7	58.6	5.4	57.0	29.3
MADGNet (CVPR2024)	14.8	19.5	6.5	32.3	16.0	11.5	2.3	13.4	17.2
TransGUNet (Ours)	47.2	52.9	20.5	51.5	59.9	73.3	17.0	63.7	38.8
	+11.4	+22.9	+3.9	+7.4	+12.1	+9.0	+11.3	+6.7	+9.5

Table 16. Segmentation results on **Multi-organ Segmentation** with *DSC*. We train each model on Synapse [3] train dataset and evaluate on Synapse [3] and AMOS-CT/MRI [28] test datasets.

Method	Synapse \Rightarrow Synapse								
	Average	Aorta	Gallbladder	Left Kidney	Right Kidney	Liver	Pancreas	Spleen	Stomach
UNet (MICCAI2016)	58.9	73.1	35.3	62.5	60.8	85.1	32.4	68.2	54.1
UNet++ (DLMIA2018)	69.8	78.0	53.3	72.6	69.2	89.5	46.4	82.7	67.0
CENet (TMI2019)	64.6	68.9	43.4	71.1	67.2	88.9	33.1	78.4	65.9
TransUNet (arxiv2021)	67.2	71.8	46.3	73.2	67.6	89.4	48.0	80.3	60.7
MSRFNet (BHI2022)	67.6	78.1	47.7	74.1	63.8	89.9	43.2	80.9	62.8
DCSAUNet (CBM2023)	59.8	68.8	41.8	64.4	57.4	86.5	32.2	73.9	53.2
M2SNet (arxiv2023)	67.5	74.1	45.5	70.4	67.9	90.3	42.0	81.2	68.7
PVT-GCASCADe (WACV2024)	68.9	75.0	47.5	74.0	70.1	90.4	39.9	80.5	73.5
CFATransUNet (CBM2024)	70.4	76.2	47.7	75.4	73.0	90.9	48.0	80.8	71.3
MADGNet (CVPR2024)	69.8	73.0	48.7	75.8	71.9	90.4	45.7	80.2	72.9
TransGUNet (Ours)	71.4	76.4	48.7	79.4	76.0	91.1	43.9	81.6	74.0
	+0.9	-1.6	-4.6	+3.6	+3.0	+0.2	-4.1	-1.1	+1.1
Method	Synapse \Rightarrow AMOS-CT								
	Average	Aorta	Gallbladder	Left Kidney	Right Kidney	Liver	Pancreas	Spleen	Stomach
UNet (MICCAI2016)	44.8	49.3	33.2	39.0	42.3	74.9	17.2	57.0	45.5
UNet++ (DLMIA2018)	56.6	54.4	51.9	54.4	54.7	80.2	30.5	68.3	58.1
CENet (TMI2019)	56.5	59.7	40.0	58.5	61.1	81.9	27.3	68.7	54.7
TransUNet (arxiv2021)	57.7	63.6	49.0	55.0	57.4	83.3	26.9	69.2	57.5
MSRFNet (BHI2022)	51.3	58.4	43.7	47.3	44.2	79.1	22.5	65.4	49.7
DCSAUNet (CBM2023)	36.3	32.4	22.9	25.0	31.4	75.4	11.8	56.4	34.9
M2SNet (arxiv2023)	58.5	62.0	49.0	55.7	58.2	84.2	28.6	69.9	60.6
PVT-GCASCADe (WACV2024)	58.5	57.5	45.0	54.3	60.9	85.6	28.9	72.8	62.9
CFATransUNet (CBM2024)	56.7	62.4	40.9	56.0	63.5	80.2	30.4	67.7	52.5
MADGNet (CVPR2024)	64.4	68.2	52.0	68.3	65.5	84.1	37.6	74.2	65.6
TransGUNet (Ours)	66.2	69.8	50.6	70.1	73.3	86.0	36.8	76.1	66.5
	+1.7	+1.6	-1.4	+1.8	+7.8	+0.4	-0.8	+1.9	+0.9
Method	Synapse \Rightarrow AMOS-MRI								
	Average	Aorta	Gallbladder	Left Kidney	Right Kidney	Liver	Pancreas	Spleen	Stomach
UNet (MICCAI2016)	5.3	3.5	5.3	1.7	8.8	16.6	0.6	3.2	2.8
UNet++ (DLMIA2018)	3.8	5.9	6.0	5.0	1.6	3.8	0.8	2.9	4.2
CENet (TMI2019)	9.0	8.1	5.6	14.1	22.3	8.0	3.1	5.5	5.3
TransUNet (arxiv2021)	5.8	5.9	6.9	12.2	13.3	4.1	1.0	1.8	1.5
MSRFNet (BHI2022)	4.2	2.6	6.9	3.7	3.0	8.5	1.4	2.4	4.9
DCSAUNet (CBM2023)	1.1	0.5	1.7	0.0	0.4	4.8	0.0	1.0	0.2
M2SNet (arxiv2023)	14.7	20.2	7.0	24.7	24.1	17.8	2.8	11.4	9.8
PVT-GCASCADe (WACV2024)	24.3	17.4	9.4	33.6	35.8	50.4	2.2	29.6	15.9
CFATransUNet (CBM2024)	25.9	21.1	13.1	31.0	36.1	42.6	2.9	41.9	18.5
MADGNet (CVPR2024)	9.8	12.5	5.8	22.1	10.3	6.5	1.2	9.5	10.2
TransGUNet (Ours)	35.6	39.0	14.7	40.5	46.1	59.5	9.5	49.3	25.8
	+9.6	+17.9	+1.6	+6.9	+10.0	+9.1	+6.4	+7.4	+7.3

Table 17. Segmentation results on **Multi-organ Segmentation** with *mIoU*. We train each model on Synapse [3] train dataset and evaluate on Synapse [3] and AMOS-CT/MRI [28] test datasets.

Method	Synapse \Rightarrow Synapse								
	Average	Aorta	Gallbladder	Left Kidney	Right Kidney	Liver	Pancreas	Spleen	Stomach
UNet (MICCAI2016)	43.8	15.1	46.8	45.6	90.6	28.3	21.5	76.6	26.2
UNet++ (DLMIA2018)	34.9	4.3	52.5	51.2	62.2	20.4	11.4	61.5	15.6
CENet (TMI2019)	39.8	13.5	86.5	53.8	86.8	16.4	13.8	21.6	25.9
TransUNet (arxiv2021)	34.3	10.7	53.8	37.0	76.5	15.0	8.1	55.3	17.7
MSRFNet (BHI2022)	38.2	8.8	56.1	59.5	66.1	26.8	13.3	36.2	38.7
DCSAUNet (CBM2023)	38.6	10.4	80.0	54.9	49.4	26.0	15.7	52.4	20.2
M2SNet (arxiv2023)	25.4	5.7	27.7	49.6	48.0	22.4	10.9	25.7	13.5
PVT-GCASCADe (WACV2024)	18.8	5.6	20.2	25.5	36.0	17.8	12.9	20.8	11.6
CFATransUNet (CBM2024)	18.8	5.6	29.0	16.0	34.6	23.1	10.8	20.1	10.8
MADGNet (CVPR2024)	24.9	5.7	29.8	40.4	44.1	14.0	13.2	35.0	17.0
TransGUNet (Ours)	23.4	7.1	33.6	14.6	48.3	22.4	70.5	39.8	10.8
	-4.6	-1.5	-13.4	+1.4	-13.7	-8.4	-2.4	-19.7	+0.0
Method	Synapse \Rightarrow AMOS-CT								
	Average	Aorta	Gallbladder	Left Kidney	Right Kidney	Liver	Pancreas	Spleen	Stomach
UNet (MICCAI2016)	72.1	39.5	83.5	94.1	132.4	36.8	24.5	129.7	36.5
UNet++ (DLMIA2018)	43.9	19.9	55.0	73.4	45.7	25.5	16.9	90.5	24.0
CENet (TMI2019)	52.2	13.5	97.5	53.3	106.2	24.1	27.0	55.5	40.1
TransUNet (arxiv2021)	39.5	15.4	46.2	46.1	102.3	19.6	21.6	40.1	25.0
MSRFNet (BHI2022)	47.0	20.2	31.8	96.6	49.2	22.6	26.3	90.9	38.4
DCSAUNet (CBM2023)	50.5	28.7	92.1	63.1	82.9	23.4	34.6	44.7	34.5
M2SNet (arxiv2023)	41.2	10.0	30.8	73.7	72.9	22.0	20.3	69.8	29.7
PVT-GCASCADe (WACV2024)	27.5	12.8	35.9	46.5	40.2	13.9	21.9	27.7	20.9
CFATransUNet (CBM2024)	46.3	14.9	81.0	84.3	54.1	27.1	24.7	59.0	24.9
MADGNet (CVPR2024)	31.2	10.0	34.7	58.5	55.7	16.8	18.6	29.2	26.2
TransGUNet (Ours)	24.4	72.5	37.1	29.6	46.3	13.5	15.7	27.1	19.1
	+1.8	-2.5	-0.3	+16.5	-6.1	+0.4	+1.2	+0.6	+1.8
Method	Synapse \Rightarrow AMOS-MRI								
	Average	Aorta	Gallbladder	Left Kidney	Right Kidney	Liver	Pancreas	Spleen	Stomach
UNet (MICCAI2016)	190.3	144.3	198.4	143.0	187.3	198.4	105.9	322.0	223.2
UNet++ (DLMIA2018)	169.3	68.9	248.7	109.0	134.2	207.7	113.0	264.1	209.0
CENet (TMI2019)	182.8	95.9	242.6	171.4	143.1	216.3	157.0	267.1	168.9
TransUNet (arxiv2021)	162.3	100.6	256.8	114.3	160.9	199.3	116.4	237.4	112.8
MSRFNet (BHI2022)	166.3	102.4	166.1	144.0	137.0	178.6	136.9	210.9	254.4
DCSAUNet (CBM2023)	147.2	124.1	108.7	230.1	183.4	97.1	86.4	194.8	152.6
M2SNet (arxiv2023)	131.7	55.4	148.8	130.7	136.9	153.0	90.0	203.3	135.6
PVT-GCASCADe (WACV2024)	110.5	62.4	115.4	127.4	141.0	91.0	74.5	150.0	122.1
CFATransUNet (CBM2024)	115.6	69.2	146.2	156.3	137.0	108.3	57.4	171.3	79.2
MADGNet (CVPR2024)	128.2	71.7	121.0	148.4	144.6	149.9	79.9	199.5	110.7
TransGUNet (Ours)	98.7	45.2	123.4	105.2	136.8	97.2	60.7	142.0	84.9
	+11.8	+10.2	-14.7	+3.8	+0.2	-0.2	-3.3	+8.0	-5.7

Table 18. Segmentation results on **Multi-organ Segmentation** with *HD95*. We train each model on Synapse [3] train dataset and evaluate on Synapse [3] and AMOS-CT/MRI [28] test datasets.